The Interaction of Katabatic Flow and Mountain Waves. Part II: Case Study Analysis and Conceptual Model

GREGORY S. POULOS

National Center for Atmospheric Research, Earth Observing Laboratory, Boulder, Colorado*

JAMES E. BOSSERT

Los Alamos National Laboratory, Los Alamos, New Mexico

THOMAS B. MCKEE AND ROGER A. PIELKE SR.

Colorado State University, Fort Collins, Colorado

(Manuscript received 6 February 2006, in final form 21 September 2006)

ABSTRACT

Via numerical analysis of detailed simulations of an early September 1993 case night, the authors develop a conceptual model of the interaction of katabatic flow in the nocturnal boundary layer with mountain waves (MKI). A companion paper (Part I) describes the synoptic and mesoscale observations of the case night from the Atmospheric Studies in Complex Terrain (ASCOT) experiment and idealized numerical simulations that manifest components of the conceptual model of MKI presented herein. The reader is also referred to Part I for detailed scientific background and motivation.

The interaction of these phenomena is complicated and nonlinear since the amplitude, wavelength, and vertical structure of the mountain-wave system developed by flow over the barrier owes some portion of its morphology to the evolving atmospheric stability in which the drainage flows develop. Simultaneously, katabatic flows are impacted by the topographically induced gravity wave evolution, which may include significantly changing wavelength, amplitude, flow magnitude, and wave breaking behavior. In addition to effects caused by turbulence (including scouring), perturbations to the leeside gravity wave structure at altitudes physically distant from the surface-based katabatic flow layer can be reflected in the katabatic flow by transmission through the atmospheric column. The simulations show that the evolution of atmospheric structure aloft can create local variability in the surface pressure gradient force governing katabatic flow. Variability is found to occur on two scales, on the meso-β due to evolution of the mountain-wave system on the order of one hour, and on the microscale due to rapid wave evolution (short wavelength) and wave breaking–induced fluctuations. It is proposed that the MKI mechanism explains a portion of the variability in observational records of katabatic flow.

1. Introduction

We describe results from an investigation of the interaction of katabatic flows in the nocturnal boundary layer (NBL) with topographically forced gravity waves. We will refer to this phenomenon as mountain wave–katabatic flow interaction (MKI). A companion paper (Poulos et al. 2000), which is hereafter referred to as Part I, gives a historical review of relevant literature, describes our scientific motivation and the experimental site, presents the case night observations in detail, and analyzes a series of idealized numerical simulations. The conclusions in Part I are reinforced herein with a case study from the Atmospheric Studies in Complex Terrain (ASCOT) 1993 field program and high-resolution, three-dimensional, realistic topography, numerical simulations with the Regional Atmospheric Modeling System (RAMS). The reader is re-

* The National Center for Atmospheric Research is sponsored by the National Science Foundation.

Corresponding author address: Gregory S. Poulos, NCAR-EOL, P.O. Box 3000, Boulder, CO 80307-3000.
E-mail: gsp@ucar.edu

DOI: 10.1175/JAS3926.1

ferred to Poulos (1996) for detail beyond that presented in Parts I and II and a large amount of additional information related to the subject.

We focus first on introductory material and then, because of the complex nature of the nonlinear interaction and the less familiar analysis tools used, we focus primarily on detailed numerical analysis of MKI from the three sensitivity studies. Section 2 briefly describes the case night of interest (0000–1200 UTC 4 September 1993), focusing on the aspects relevant to katabatic flow and mountain waves. Section 3 presents the design of the three-dimensional numerical experiments, including details of the model setup and a description of the outcome of the three sensitivity tests. Section 3 also briefly reviews from Poulos (1996) how the model output from a realistic 12-h simulation (called REAL) compares to observations taken from the 1993 ASCOT field experiment. Following Stein and Alpert (1993), we then describe the results of two sensitivity simulations, one with radiative forcing only (called the katabatic flow–only simulation or KFO) and one with dynamic forcing but without radiation (called the mountain wave–only simulation or MWO). MKI, being a nonlinear phenomenon and generating occasionally rapid fluctuations, is not readily evaluated using exclusively traditional cross-sectional and plan view plots from numerical simulations. Therefore, in section 4, we use $2\Delta t$ time series intercomparisons of meteorological fields and terms of the u-component force balance between the three simulations to extract qualitative and quantitative information about the interaction of mountain waves and katabatic flow in the NBL. Section 5, drawing on the conclusions of Parts I and II combined, describes the resulting conceptual model of MKI and concludes the manuscript with final remarks.

2. Case night description in brief

The focus area for the 1993 ASCOT experiment was the eastward-facing slope of the northern Colorado Rocky Mountains, from the Continental Divide crest down to the mountain–plains interface. This slope is subdivided into generally east–west-oriented canyons, and the ASCOT field observations during the night of interest to this study were focused on Eldorado Canyon, Coal Creek Canyon, and the nearby plain (Part I, Fig. 2).

The overnight period of 0000–1200 UTC 4 September 1993 in north central Colorado was dominated by clear skies due to the synoptic influence of a high pressure system whose center was located to the southwest of the ASCOT study area, as described in detail in Part I. In combination with synoptic low pressure to the northeast, large-scale dynamics generated geostrophic northwesterly flow aloft. The 915-MHz wind profiler at Gross Reservoir (see location in Fig. 2 of Part I) indicated west to northwest winds of 10–15 m s^{-1} on the east side of the Continental Divide in the Eldorado Canyon drainage up to 5 km AGL. Based on mean horizontal wind speed, U, and stability based on the Brunt–Väisälä frequency, $N = g\partial\theta/\theta\partial z$, in the 2–4 km ($H = 2000$ m) mean sea level (MSL) layer of the Grand Junction 0000 and 1200 UTC soundings on the upwind side of the barrier, the Froude number, Fr, was ~0.45 overnight, where Fr $= U/NH$. Thus, nonlinear gravity wave behavior is expected (Queney et al. 1960; Queney 1948; Baines 1979; Smith 1979, 1989; Olafsson and Bougeault 1996) if we assume that the mean value of Fr can be considered a satisfactory representation of relevant flow conditions (cf. Durran 1990). In the context of the significant half-width of the Rocky Mountain barrier, the large-scale flow was hydrostatic, although local-scale peaks and valleys complicate the evolution with nonhydrostatic effects for the given U and N (Durran 1990). The wind direction was consistent −319° at both sounding times with an average wind speed of 8.6 and 6.5 m s^{-1} for 0000 and 1200 UTC, respectively. Within this same layer and over the same period, atmospheric stability dropped from $\partial\theta/\partial z = 1.6$ K km^{-1} to $\partial\theta/\partial z = 1.0$ K km^{-1} (less stable than the U.S. Standard Atmospheric stability of $\partial\theta/\partial z = 3.4$ K km^{-1}). Based on this analysis, we expect that mountain-wave flow would penetrate close to the surface but be hindered on approach of the surface by strong, near-surface statically stable layers driven by nocturnal cooling as shown in Part I.

That this was the case is supported by the 2–5 m s^{-1} winds that prevailed in the very lowest 10 m of the atmosphere by the tower measurements from the National Center for Atmospheric Research (NCAR) Mesonet, the ASCOT campaign intra- and extracanyon surface array, and the Boulder Atmospheric Observatory (BAO) operated by the National Oceanic and Atmospheric Administration (NOAA). The BAO is located about 20 km east of the base of Eldorado Canyon and, for example, indicated wind speeds varying around 5 m s^{-1} at higher levels (50–250 m AGL) and around 3 m s^{-1} at the 10-m level and a stable thermal profile (Poulos 1996). At BAO, wind direction was easterly prior to the onset of katabatic flow, westerly in the early stages of katabatic flow, and gradually turned to the north and northeast by 0400 mountain standard time (MST). The late night northward turn of the wind could be due to the slightly eastward shift of the lee trough location, causing the BAO to reside in geostrophic northerly forcing, or possibly a result of the Coriolis

force. The timing of wind direction transitions was highly variable within the ASCOT network; however, some areas, such as low levels in Coal Creek Canyon, experienced continuous westerly winds.

3. Experimental numerical modeling

For the numerical analysis presented here, the Regional Atmospheric Modeling System (RAMS) was used. It is a three-dimensional, prognostic, primitive equation mesoscale model formulated in nonhydrostatic, compressible form and its many features are thoroughly described in Pielke et al. (1992). For initialization, the NOAA/Forecast Systems Laboratory's (NOAA/FSL) 6-hourly gridded Mesoscale Analysis and Prediction System (MAPS) analyses were used (Bleck and Benjamin 1993; Pan et al. 1994). These volumes of atmospheric data, which have 60-km horizontal grid spacing, provide an objective initial field and external boundary condition in the RAMS model in four-dimensional data assimilation (4DDA) mode. The observations that comprise the MAPS data come from a number of sources, including the NCAR Mesonet, radar, wind profilers, aircraft observations, or standard National Weather Service (NWS) observations. In the simulations where MAPS data are used with 4DDA, only the outermost five grid points of the coarsest grid (Fig. 1) are nudged.

a. Simulation types

Since our interest is the nonlinear interaction of two phenomena, mountain waves and katabatic flows, it is important to ensure that the sensitivity studies chosen will, indeed, extract that information. Following the sensitivity study formalism of Stein and Alpert (1993) with two factors, 1) katabatic flow, whose existence in this case is dictated by clear-sky radiative cooling and 2) mountain waves caused by flow over topography initialized from MAPS volumes, four simulations (2^2) are required. These are 1) both MAPS nudging and the radiation parameterization active (henceforth, REAL, for realistic simulation), 2) the radiation parameterization active, but with initial $U = 0$ (henceforth, KFO, for katabatic flow–only simulation), 3) the MAPS nudging only without the radiation parameterization active (henceforth, MWO, for the mountain wave–only simulation), and 4) neither MAPS nudging nor the radiation parameterization active. Since the latter simulation results in steady-state, quiescent conditions it is the null case and only three simulations are required.

b. Model configuration

The temporal and spatial scales relevant to katabatic flow and mountain waves determine both the grid spacing and domain extent required to simulate the phenomena credibly (Figs. 1 and 2). The relevant horizontal scale for the evolution of mountain waves in a real case study is considerably larger than for idealized cases where the upstream flow can be specified. For realistic cases the distance a synoptic disturbance, whose U and N evolution determines gross mountain-wave behavior, would travel during the overnight period is minimally required on either side of the domain center. The vertical wavelength of a topographically forced wave in this part of the Rocky Mountains, λ_z, can be approximated conservatively as 4 km (cf. Lee et al. 1989). Using the above scales, and a benchmark of 10 grid increments to resolve features adequately, the outermost of

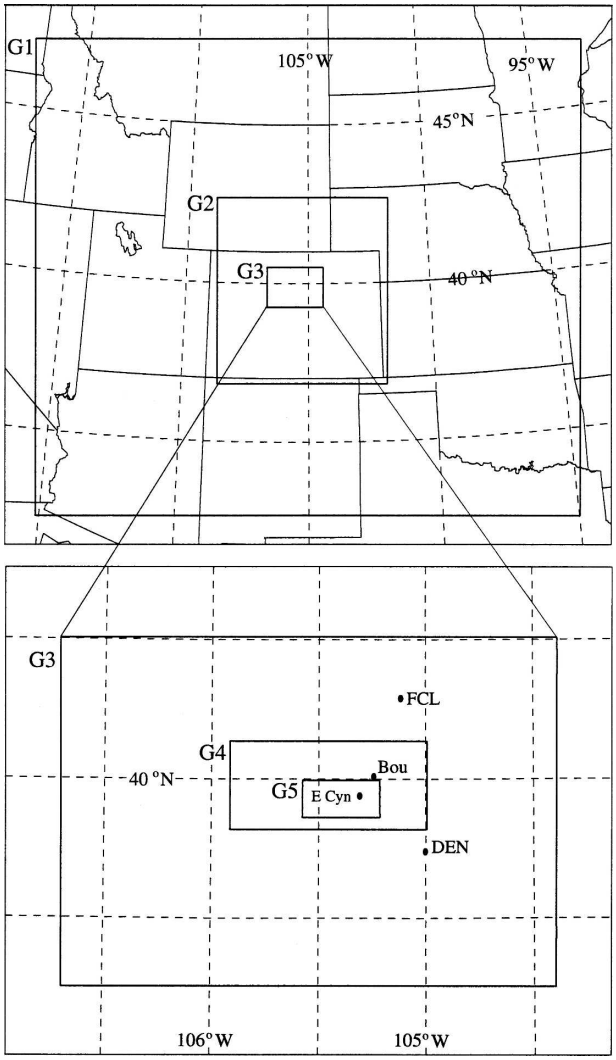

FIG. 1. The five grids used in our simulations. Grid 3 is shown in both the upper and lower portions of the figure for reference. Note that the grids sequentially telescope down to the region of interest on grid 5 (see also Fig. 2), which overlies Eldorado Canyon and the ASCOT study region.

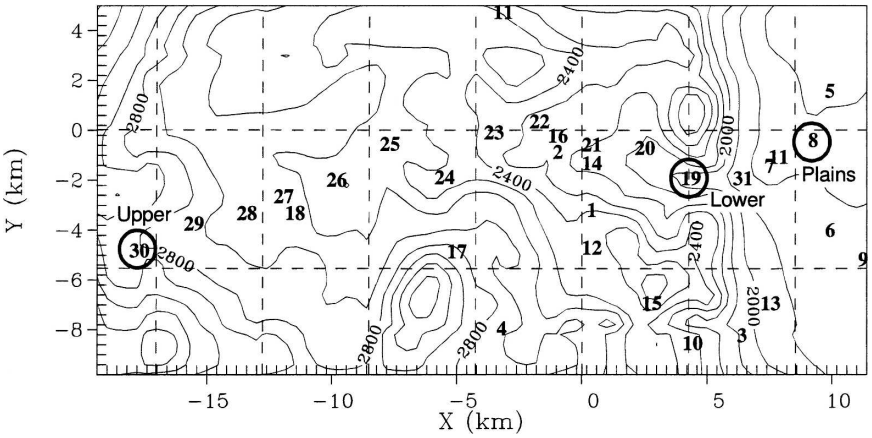

FIG. 2. RAMS topographical representation of the innermost of five grids (grid 5) used in the numerical simulations described herein. The southwest corner is at 39.86°N, 105.58°W with increments (dashed lines) of 0.05° and topographic contours every 100 m. Numerals 1–31 indicate specific grid points where meteorological variables and their forcings were extracted every 120 s ($2\Delta t$) of simulated time, with focal points in the upper and lower canyon and plains encircled.

the three-dimensional five-grid configuration (see Fig. 1) is $\Delta x = \Delta y = 57.6$ km and $\Delta z = 60$ m. Above 1000 m AGL, stretching was applied such that Δz gradually increased to $0.1\lambda_z$. Grids 2–4 (see Fig. 1) used sequential horizontal grid nesting ratios of 3:1, 4:1, and 3:1, respectively, but the same vertical grid structure as grid 1. Grids 2 and 3 encompass large-scale terrain features that can influence mountain-wave evolution, the entire state of Colorado and the north central Colorado Rockies, respectively. Grid 4 crosses the Continental Divide west of Eldorado Canyon with a 1.6-km horizontal grid interval while also extending well onto the plains around Rocky Flats. Grid 4 is intended to capture mountain-wave structure with considerable detail as air passes over the Continental Divide and descends upon the canyons of interest. The fifth and innermost grid (see Figs. 1 and 2) was nested at a 4:1 ratio such that $\Delta x = \Delta y = 400$ m and captures the canyon orography in which katabatic flows and MKI would develop in Eldorado Canyon. The vertical scale of katabatic flows (~400 m jet maximum; Banta et al. 1995, 1996) suggested $\Delta z_{\min} = 40$ m, but $\Delta z = 20$ m was implemented in the lowest 800 m AGL via vertical grid nesting such that shallower flows in Coal Creek Canyon and the nascent stages of Eldorado Canyon flows might be better realized (see Fig. 3). Care was taken to ensure that vertical stretch ratios were close enough to 1.0 to retain accuracy in vertical differencing. Grid 5 encompasses the majority of Eldorado Canyon's drainage area but does not cross the Continental Divide. All grids have a domain depth over 17-km MSL. Figure 2 is annotated to indicate the locations *nx*, *ny* where meteorological and model forcing information was extracted every 2 min at each grid point in the column. (Figures 8–12 and 14 show data derived from these special extraction points, which were used in concert with spatial cross sections and the results of Part I to generate the conceptual model presented.)

Other model parameters were chosen to be as realistic as possible to the case night of interest and those that would be required to reproduce these results are shown in Table 1. The simulation length was chosen to be 12 h, beginning near sunset before the case night (0000 or 0100 UTC). We have found that in the simulation of katabatic flows the two most effective start times are at the morning and evening transitions. At these times the ground and near-surface air temperature are often close and an atmospheric stability transition often occurs. For the first hours of simulated time the model adjusted to the initial conditions, and this impact appears in forthcoming figures.

c. The mountain wave–katabatic flow interaction simulation (REAL)

The goal of this simulation was to recreate the 4 September 1993 case night conditions as well as possible. Given an accurate representation of the observed large-scale conditions and a qualitatively representative simulation of actual atmospheric variability at the mesoscale for the phenomena of interest, we then analyze the detailed information available from the numerical model to explain the evolution of flow phenomena in section 4. Clearly, since the outer domain of grid 1 was nudged with the MAPS dataset, one expects the grid 1

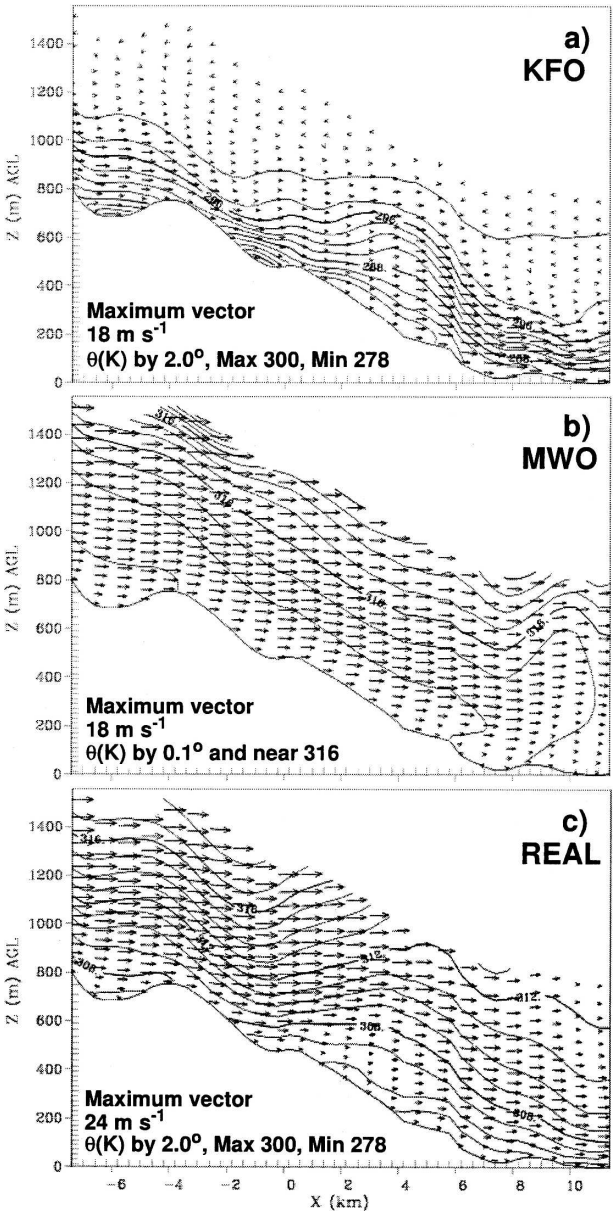

FIG. 3. An intercomparison of the MKI sensitivity tests in lower Eldorado Canyon. Horizontal wind vectors and θ in the x–z plane (400 m south of line A in Fig. 4; $y = -2.2$ km) at 0700 UTC 4 Sep 1993 for (a) KFO, (b) MWO, and (c) REAL are shown.

model solution from REAL to well represent the synoptic-scale observations for this case night. In the interior of the outermost domain and on interior grids, where 4DDA is not active, however, such a comparison is not assured. In the case of very small scale grids (see Fig. 4), much smaller scale terrain-induced flow features are capable of being simulated, but the influence of subgrid-scale roughness, vegetation, turbulence, and soil characteristics on flow variability is not expected to be represented.

TABLE 1. Model configuration details for ASCOT case study and sensitivity simulations abbreviated KFO, MWO, and REAL.

Characteristic	Configuration
No. of grids and grid points per grid	5; the number of grid points in the x, y, and z directions were $34 \times 30 \times 69$, $32 \times 35 \times 69$, $42 \times 30 \times 69$, $50 \times 23 \times 69$, and $78 \times 38 \times 86$ on grids 1–5, respectively.
Simulation length	12 h
Domain focus area	Northern Colorado Rocky Mountain barrier and Eldorado Canyon
Output	Meteorological variables and balance equation terms at specific points
Initial time and date	0000 UTC 4 Sep 1993 (0500 LST 3 Sep 1993)
Initialization	Horizontally homogeneous, quiescent, or with MAPS data
Terrain data resolution	30 s (−800 m) on grids 1–3; 3 s (−80 m) on grids 4 and 5
Turbulent diffusion	Vertical: level 2.5; horizontal: K theory
Lateral boundaries	Klemp and Wilhelmson (1978) radiative or nudged (MAPS)
Vertical boundaries	Top: lid with 10 absorbing layers or nudged; Bottom: no slip
Roughness length	As derived from vegetation dataset
Radiation	Short- and longwave parameterization (updated every 600 s)
Soil (parameterized)	11 layers; silty clay loam; 30% of saturation
Vegetation (parameterized)	From geographic dataset in 30-s increments

Toward the purpose of familiarizing the reader with REAL and how it differs from the idealized sensitivity studies (described below) Fig. 3 presents a vertical cross section through lower Eldorado Canyon from each simulation. In Fig. 3c, we find that a wavelike feature of $\lambda \approx 5$ km has formed on the western side of the lower canyon and $N > 0$ throughout the canyon atmosphere to 1500 m AGL. Since radiative forcing and topographically induced gravity waves are influencing the flows here and as evidenced by intercomparing Figs. 3a–c, it is not possible to classify the REAL flow realization as entirely mountain waves or katabatic flows. In fact, as the upcoming descriptions will show and as shown in Part I, these flows nonlinearly interact to create an atmospheric evolution far different than either KFO or MWO.

REAL is also intended to represent with some fidelity the actual atmospheric evolution on the case night in question. Based on the detailed intercomparisons of the modeled results and observations in Poulos (1996), we conclude that the model prognosis of actual atmospheric conditions for the 3–4 September 1996 case

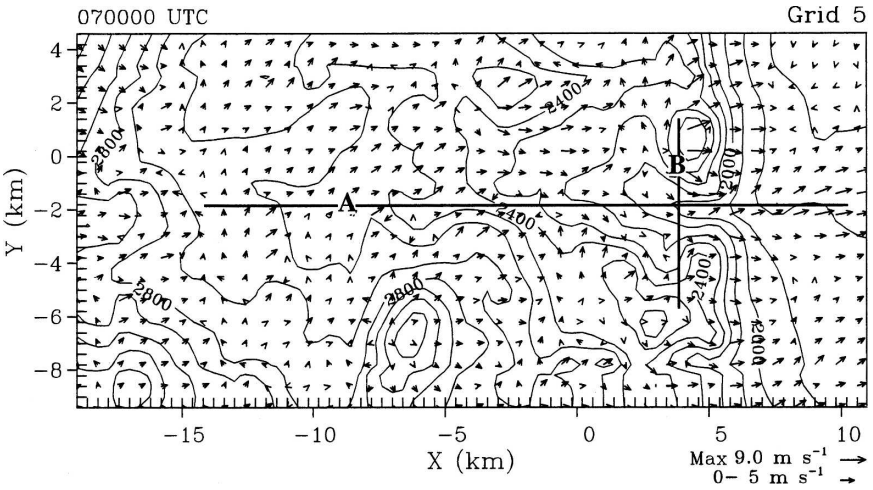

FIG. 4. Horizontal wind vectors and topography (100-m contours) for 50 m AGL at 0700 UTC of the 3–4 Sep 1993 case night for the idealized, no wind initialization (KFO). All flows are katabatic. The lines labeled A and B indicate the location of the cross sections in Figs. 5 and 6, respectively.

night is satisfactory. Large-scale atmospheric features, such as described in section 2, were well predicted. Mesoscale and local atmospheric phenomena were captured sufficiently on the innermost grids, such as mountain-wave and katabatic flows, in particular. In addition to inadequacies in the initial condition and the necessary use of parameterization, poorly predicted conditions could be explained by the imperfect terrain representation in the model and subsequent misrepresentation of terrain forcing at certain locations. Overall, the model performance is sufficiently good to give confidence that the majority of the relevant physical and dynamic mechanisms have been captured and that analysis of those mechanisms will be valid. On this basis, and because extensive time series analysis of REAL is presented in section 4, further analysis herein is deferred.

d. The katabatic flow–only simulation

This simulation was run with the same configuration as REAL, except that the initialization was horizontally homogeneous using the potential temperature (θ) profile extracted from the Grand Junction sounding and initially quiescent (e.g., Bossert and Poulos 1995; Poulos and Bossert 1995). The simulation began at 0100 UTC 4 September to ensure that radiative cooling took effect immediately. The results from this simulation therefore represent the katabatic flows that would have developed on this case night had all winds suddenly become zero near the surface at sunset. KFO gives us important insights about the dynamics of complex terrain katabatic flows, while also showing the likely maximum katabatic flow scenario for the Eldorado Canyon region for the given atmospheric stability (see Figs. 3a and 4). The following analysis forms the basis from which differences with MWO and in particular, REAL, will be evaluated in our investigation of MKI.

The katabatic flows generated by radiative cooling in this simulation were qualitatively and quantitatively realistic given the underlying terrain and the measurements during the ASCOT field experiment, with one main exception. That is, after approximately 6 h of simulated time (0700 UTC) unrealistic cooling began to develop at certain grid points on grid 5. Some of these problem areas were in the middle of the east–west extent of Eldorado Canyon, and thus the cold air was advected over other down-canyon and plains locations by 8 h of simulated time. The following discussion therefore focuses on the first 6 h of KFO (note that the unrealistic cooling error originated from a localized point and therefore did not significantly impact vertical integrals taken at different points in KFO, see section 4a). Note that this problem did not arise in either MWO or REAL, and it is unclear exactly where the model problem originates from. Preliminary analysis has narrowed the error down to an interaction between the turbulent diffusion and surface layer parameterizations that causes very high cooling rates during statically stable, weak wind conditions. This is not an unknown problem (Poulos and Burns 2003) and has been ascribed to a variety of sources as noted, for example, by Derbyshire (1999), Viterbo et al. (1999), and Mahrt (1998).

Katabatic wind speeds achieved their maximums by

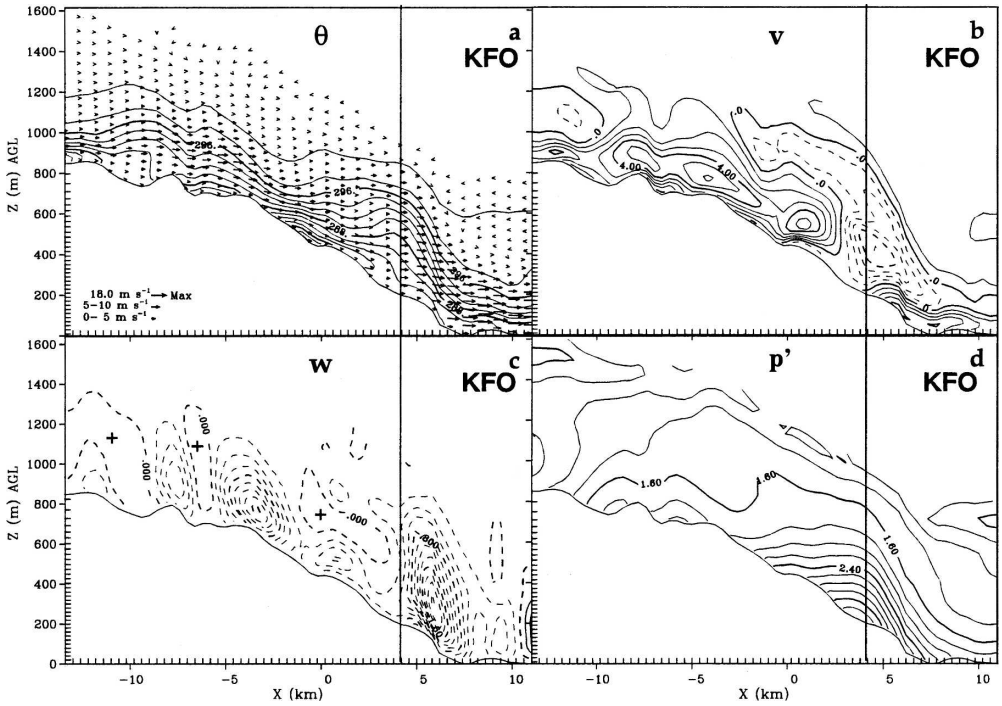

FIG. 5. Four east–west vertical cross sections down the center of Eldorado Canyon at 0700 UTC (0000 MST) from KFO (see the line labeled A in Fig. 4 for location; $y = -1.80$ km): (a) θ in 2.0-K intervals with wind vectors, (b) cross-canyon or v in 1.0 m s^{-1} intervals, (c) w in 0.20 m s^{-1} intervals, and (d) p' in 0.2-hPa intervals. The vertical line at $x = 4.2$ km shows the cross section location of Fig. 6.

~5 h after initialization and their evolution thereafter was nonsteady. Figure 3a shows that large N developed by this time up to 300 m AGL, within which strong (18 m s^{-1} at $x \approx 9$ km) katabatic flows, jets, and theorized antiwinds (Buettner and Thyer 1965) correspondingly occur. Figure 4 shows the horizontal flow field at 0700 UTC for 50 m AGL. The winds mostly follow terrain gradients or are down-valley as expected and are relatively light compared to the winds just above this level. The maximum wind is evident just east of the exit of Eldorado Canyon where katabatic flows become shallower compared to those within the constrained portion of the canyon (Fig. 3a). Outer grids (not shown) are also dominated by katabatic flow. Coal Creek Canyon, which is oriented parallel to Eldorado Canyon but approximately 15 km to its south, also contains katabatic flow; it is weaker and shallower than that in Eldorado Canyon, as was typically observed during ASCOT (see Part I). The slower speeds are most likely due to the smaller air shed and depth of Coal Creek Canyon but may also be partly the result of somewhat worse topographical representation of Coal Creek Canyon by the given dataset and chosen grid spacing.

The strong flow over the mountain just north of Eldorado Canyon (Fig. 4, $x = 5$ km, $y = 0$ km) was investigated because katabatic flows would not normally be expected to exist at a local topographic maximum. An analysis of the model fields shows that this feature is the result of strong west-southwest katabatic flow generated in the upper southwest–northeast-oriented portion of Eldorado Canyon intercepting the mountain barrier. As the strong katabatic upper canyon flow approaches the clockwise turn in Eldorado Canyon (Fig. 4, $x = -5$ km, $y = 0$ km) where the topographic gradient becomes east–west oriented, its momentum causes it to continue east-northeastward. Such wind deviations have been observed and simulated for valley flows in the Riviera Valley during the Mesoscale Alpine Program (Chow et al. 2006; Weigel et al. 2006). This feature does not persist in REAL due to the altered dynamics when ambient flow and mountain waves are present. Additional analysis presented in Poulos (1996, section 6.5.1) reveals that as the katabatic flow that surmounted this local terrain maximum descends the steeper slopes to the east ($x = 7$ km, $y = 1$ km, Fig. 4) the stronger flows elevate resulting in the somewhat weaker 50-m AGL flows than at the terrain maximum itself.

A vertical cross section showing multiple variables (Fig. 5) reveals considerable detail about the lower Eldorado Canyon flow. This section is taken at midnight along an east–west line through the mouth of Eldorado

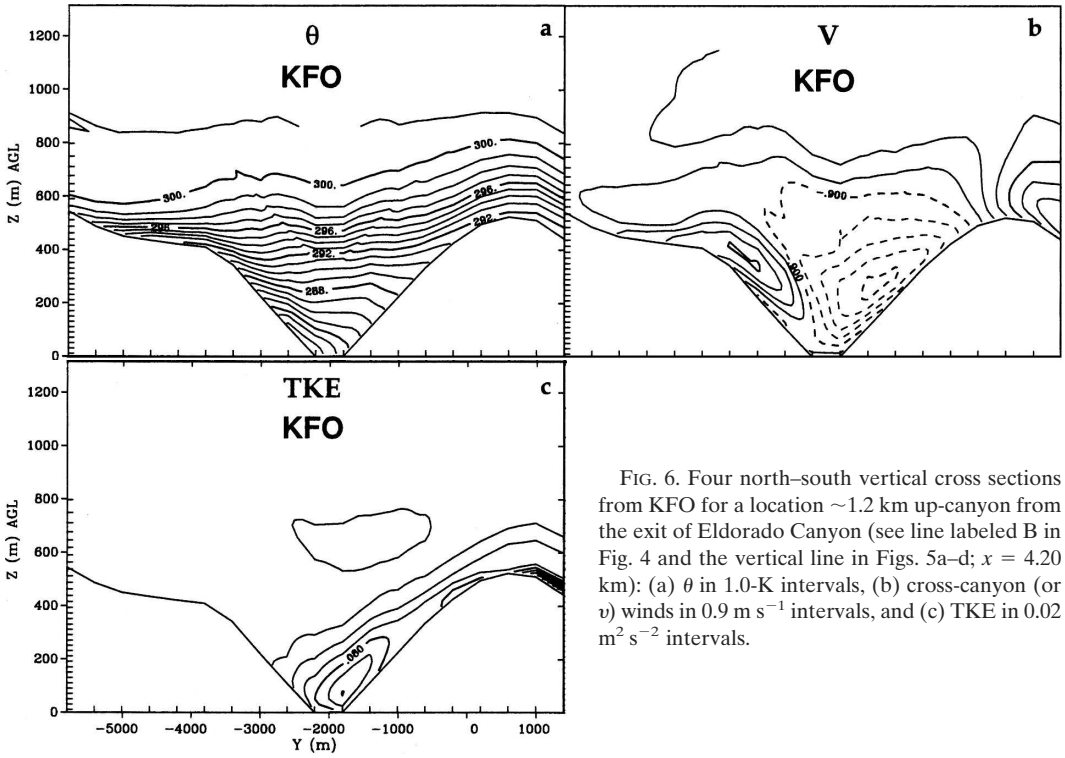

FIG. 6. Four north–south vertical cross sections from KFO for a location ~1.2 km up-canyon from the exit of Eldorado Canyon (see line labeled B in Fig. 4 and the vertical line in Figs. 5a–d; $x = 4.20$ km): (a) θ in 1.0-K intervals, (b) cross-canyon (or v) winds in 0.9 m s^{-1} intervals, and (c) TKE in 0.02 m^2 s^{-2} intervals.

Canyon (see line "A" in Fig. 4) and 400 m north of the cross section shown in Fig. 3a. Strong stratification has developed both along and across (Fig. 6a) the canyon, with the exception of the lower 200 m from $x = 2.5$–5.5 km, and katabatic flows enter and exit the lower geographically contracted portion of the canyon near 15 m s^{-1}. If one considers the converging of several individual slope and tributary flows into this canyon and that the canyon constricts in this region (see Fig. 3 and refer to Armi and Williams 1983; Saunders 1987) such speeds are reasonable. Katabatic flow near this magnitude was occasionally observed during the ASCOT campaign (Banta et al. 1995) and at times, tethersondes at the exit of Eldorado Canyon could not remain flying due to excessive wind speeds and shear out of the canyon mouth. Figure 5b shows that the velocity is well correlated with the local topographic gradient and tributary canyon inputs at low levels along this cross section. Figure 5c confirms the expected downward motion associated with pure katabatic flows, with exceptions where otherwise negatively buoyant air is forced to rise over topography or flow adiabatically along upward sloping isentropes.

A curious high-p' (perturbation pressure), low wind speed feature develops at $x = 3$–4 km in the lower levels (Figs. 5a,d) as a consequence of gap flow dynamics forced by the cold canyon-borne katabatic flow and the topographic constriction (Reed 1931; Jackson and Steyn 1994; Pan and Smith 1999; Zängl 2002). Note that p' in this figure results from the combined effects of hydrostatic and lesser nonhydrostatic changes from the initial hydrostatic reference state in the model. It is clear from Fig. 5a that the bulge of p' (3.40 hPa, Fig. 5d) coincides with the deviation of isentropes upward from the surface. Up- and down-canyon of this feature, isentropes generally slope downward. To the east of $x = 4$ km a significant katabatic flow jet forms as the canyon converges into a more narrow configuration. Near the surface upstream of the bulge, a pool of air 4–6 K colder than surrounding surface air has formed in quiescent air. The pressure gradient force (PGF) upstream of the bulge decelerates the westerly flow from 5–10 m s^{-1} to near calm for 100–200 m AGL. This calm region, without significant shear in the vertical, allows the development of the cold pool. The cold pool does not extend farther down-canyon into the high pressure region because of a local maximum in turbulent kinetic energy (TKE) (Fig. 6c) at the same location as the local high. An along-canyon section of TKE (not shown) verifies that this TKE maximum is localized.

Figure 6b provides evidence that significant $\partial v/\partial y < 0$ exists over the canyon above this point and could, in the case of a divergent flow, also have contributed to the development of this mesohigh (Song et al. 1985). Since p' increases where $\nabla \cdot \mathbf{v} < 0$, locally higher pressure could develop (u divergence was negligible). The ter-

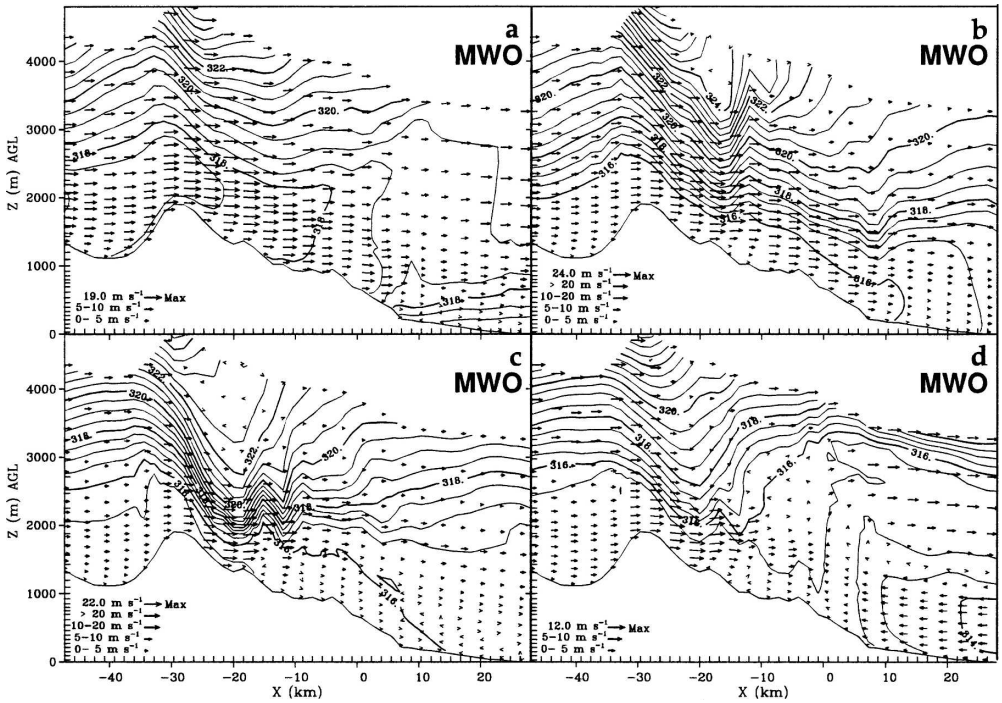

FIG. 7. East–west cross sections from MWO of θ (0.5-K intervals) and wind vectors through Eldorado Canyon on grid 4 for (a) 3, (b) 6, (c) 9, and (d) 12 h. Note the evolving mountain-wave state and cooling temperatures in time due to advection.

rain and wind field configuration shown in Fig. 4 shows that local flows converge as 1) katabatic flows from opposing slopes or tributaries meet, 2) westerly flows diverge around the mountain to the north of Eldorado Canyon (see previous section), and 3) the canyon narrows. Pan and Smith (1999), however, have shown that confluence is not the dominant mechanism in creating accelerated gap flows. The overall effects of the terrain constriction and associated mesohigh are the upward and up-canyon pressure gradients, preventing the continued downward progress and subsequent acceleration of katabatic flow. In turn, cold air flows over the local high (bulging) before accelerating and descending rapidly on the east side of the feature [$\partial p/\partial x$ = 2 hPa (7 km)$^{-1}$]. The weakened downward vertical motions, and even some upward vertical motion, are shown in Fig. 4c for the bulged region. Upward or weak vertical motions also coincide with smaller θ bulges up-canyon.

e. The mountain wave–only simulation

In MWO, where all characteristics are the same as REAL except that the radiation parameterization is not active, we expect that surface cooling will be nearly eliminated, aside from that which is nudged in and/or advected from the nudging boundaries. The upper-level synoptic-scale features of MWO (not shown) are, as expected, quite similar to those of REAL. In particular, a lee trough developed at 700 and 500 hPa of similar amplitude and location as that in REAL. The flow upstream of the Continental Divide and on grids 4 and 5 was similar to that of REAL at higher levels but noticeably different below ~500 m AGL (Fig. 3). The differences that are significant to MKI will be discussed in greater detail in the next section.

Figure 7 shows a series of vertical cross sections on a line through Eldorado Canyon across the Continental Divide on grid 4 in 3-h increments. The mountain-wave structure varies in time as flow of varying strength encounters the Rocky Mountain barrier. At 3 h of model integration (0300 UTC, Fig. 7a) a near-neutral boundary layer advects into the grid 4 domain at lower levels. Above this layer more thermally stratified air exists and mountain-wave structure is well defined. Individual isentropes descend approximately 900 m or 0.45 of the 2000-m Front Range topographic relief, which is consistent with the upstream average Froude number of 0.45. By 0600 UTC (Fig. 7b) potentially cooler air has advected into the lower domain and stronger stratification aloft causes wave amplification and reduced λ in the immediate vicinity of the peak. On a larger scale, elevated stably stratified air now extends to the eastern edge of the domain and a weaker wave feature has

developed near the mountain–plains interface. This feature is shown in more detail above $x \sim 7$ km in Fig. 3b. Weak stability is retained near the surface, as also shown in Fig. 3b (note the 0.1-K contour interval), within which wavelike features are absent. As the wave rises at $x = -15$ km, strong shear and a weak rotor form along the mountain side. Stronger flow descends to near the surface just east of the rotor. The flow on the plains remains weak. The reduction in λ continues at 0900 UTC (Fig. 6c) and wind maxima remain above 20 m s^{-1} on the east side of the Continental Divide despite weaker upstream flow. The wavelength is sufficiently contracted and upper airflow sufficiently stable that the strongest momentum in the mountain wave remains aloft east of $x = -10$ km. Unlike REAL, which developed katabatic flow 1 km east of this location due to the influence of radiative cooling, MWO exhibits weak flow. At 1200 UTC (Fig. 6d), the stratification aloft has again relaxed and λ is greater. Once again the strongest mountain-wave flow impacts are in the near-surface region just east of the Continental Divide. An easterly flow has developed over the plains in a neutral layer. Upward vertical motion and divergence aloft at $x = 0$ km indicate that a circulation has developed where the easterly plains flow and westerly mountain-wave flows converge.

4. Analyses of mountain wave–katabatic flow interaction

In the previous section we described main features of KFO, MWO, and REAL and formed a basis for the understanding of the following analysis, which reveals the nature of MKI. Here, we first intercompare our simulations using time series of u and w at two elevations above ground (similar analysis of v and θ are discussed at times but not shown). Next we evaluate vertical integrals of mass and heat flux. The majority of the analysis then focuses on the more rare and revealing analysis of components of the momentum balance equations. To give order to the analysis, three locations in the domain were chosen for discussion: 1) an upper Eldorado Canyon location close to the Continental Divide, 2) a lower Eldorado Canyon location, and 3) a plains location (points 30, 19, and 8, respectively, in Fig. 2). Still greater simplification was made for some analyses by choosing two vertical levels of the 50 available. From grid 5, model level 3 at 50 m AGL (60 m for w) was selected to represent a near-surface point likely to be under the influence of katabatic forcing, and model level 13 at 250 m AGL (260 m for w) was chosen as a vertical elevation where either katabatic forcing or mountain-wave dynamics might dominate, depending on their relative strength.

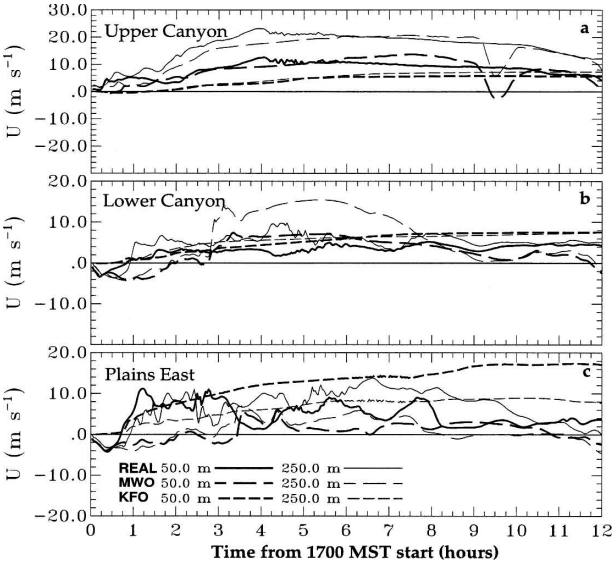

FIG. 8. Two-minute data interval, east–west component winds vs time at three different canyon-relative locations on grid 5 per Fig. 2: (a) upper canyon, (b) lower canyon, and (c) plains ~2.5 km east of Eldorado Canyon. Results are shown for REAL (solid lines), KFO (long dashes), and MWO (short dashes) at 50 and 250 m AGL; (b) is directly comparable to the momentum balances in Figs. 11, 12, and 14.

a. Time series intercomparisons by canyon-relative location and elevation

The upper canyon u (Fig. 8a) shows the expected nonlinear nature of flow evolution in the three simulations and of MKI in REAL. REAL tended toward the MWO solution at both heights, but its magnitude is obviously not additive of KFO and MWO. In the first 5 h of the simulations REAL had the strongest upper-level, upper canyon winds due to intensified stratification from radiative cooling compared to MWO (effects of stratification, Part I). While both REAL and MWO trend downward in u after 9 h, REAL does not demonstrate the significant flow reduction of MWO at 9.5 h. The v component at 250 m AGL of REAL between 2.0 and 3.75 h is northerly (during the time westerly flow is accelerating; Fig. 8a), indicative of scouring by the accelerated northwesterlies (not shown). After 4.25 h, u, v, and w (Figs. 8a and 9a) of REAL begin a period of relatively rapid variation [O(1 min.)] of their magnitude of O(1 m s^{-1}) for over an hour. This variability or gustiness corresponds with a period of increased wave amplitude, rapid wave evolution, and wave breaking aloft (see Fig. 13 and discussion in section 4c). Neither KFO nor MWO experiences this gusty period indicating that, at least for this case study, MKI had a significant impact on general flow evolution, mountain-wave development, and katabatic flow variability.

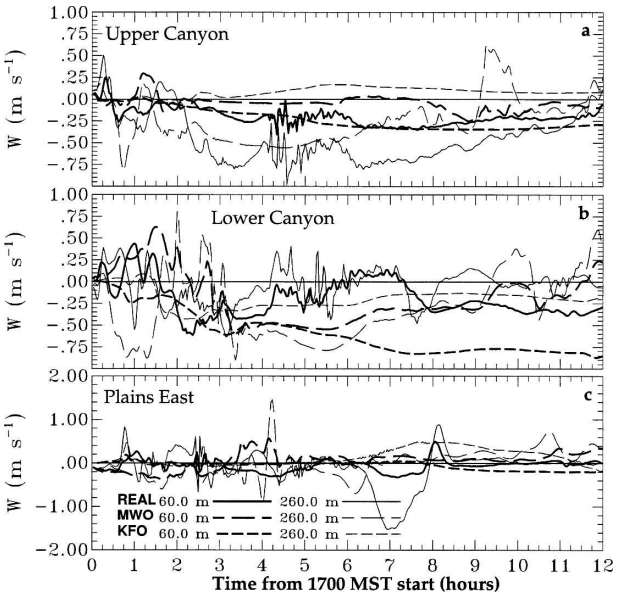

FIG. 9. Same as in Fig. 8 but for w (see Fig. 2 for locations).

The lower canyon point (Figs. 8b and 9b) is deep within Eldorado Canyon and we expect it to be dominated by katabatic flow, even when influenced by mountain waves, for two main reasons: 1) in the deeper lower canyon, cooling, and therefore the pressure gradient, is enhanced by its greater topographic amplification factor (McKee and O'Neal 1989; Whiteman 1990) and 2) the lower canyon is the most topographically sheltered location. From Fig. 8, it is immediately evident that overall horizontal velocity is lower than in the upper canyon (note the larger velocity scale in Fig. 8a), implying a degree of mechanical sheltering from mountain-wave momentum. This is partly because the grid point representing lower canyon conditions is in the vicinity of where mesoscale high pressure forms (Fig. 5d), reducing katabatic flow as described in section 3d. Just east of this point, flows accelerate to over 15 m s^{-1} in REAL and KFO as canyon topography converges further. Throughout the 12-h period, u is reasonably similar among KFO and REAL, except that in the first hour REAL experiences negative u during model spinup. This confirms the expected dominant role for katabatic forcing at this location under conditions where longwave radiative cooling is present. At 250 m AGL of MWO, relatively stronger flow persists between hours 3.5 and 8.0. This is caused by the relatively long wavelength of its mountain wave due to the lack of radiative cooling compared with REAL. Eventually, however, the wavelength of the MWO wave is reduced as flow changes induced by observational nudging influence the inner domain. Thus, after 8 h in MWO, the surface point where the mountain wave lifts off the surface is located up-canyon from this point reducing u. The mountain-wave strength during the period of strong u in MWO can also be verified by the strength of w in Fig. 8b where downward vertical motion is a local maximum.

In REAL, lower canyon winds generally remain near that of KFO because of stratification and the shortening of λ (higher altitude separation, Part I) relative to MWO. For this reason, lower canyon winds track primarily with KFO, confirming that katabatic forcing dominates mountain-wave forcing at this deep canyon location. The v component (not shown) does, however, experience a local low-level maximum between 5.0 and 7.0 h in REAL. This is caused by surface-based katabatic flows from the lower canyon's northern tributary, which are somewhat eroded by the overlying flow. In KFO, where erosion from aloft does not occur, katabatic flow is deeper after 5 h of simulated time.

From 1.0 to 11.0 h of simulated time the katabatic flow on the plains (Figs. 8c and 9c) has jet structure and is from the southwest. At 6.0 h, for instance, u at 50 and 250 m is 13.0 and 6.0 m s^{-1} (Fig. 8c), respectively, and v is 4.0 and 1.0 m s^{-1} (not shown), respectively. Clearly, a strong low-level katabatic jet exists. The reason the katabatic flow turns to the north after exiting Eldorado Canyon, particularly at low levels, is that the topographic gradient of South Boulder Creek on the plains is southwest–northeast. Note that from 6.0 to 8.0 h the katabatic flow at this point changes from a west-southwest orientation to west and then to west-northwest. This transition is accompanied by some instability and coincides with a transition to upward vertical motion, particularly at upper levels (Fig. 9c). This transition is caused by cold air exiting Eldorado Canyon at 6.0 h (see also section 3d) and a concomitant increase in inversion strength, such that katabatic flow from the foothills west of this point overrides the strong inversion without being channeled to the northeast.

By comparison, the flow over the plains in REAL is far more variable, as should be expected due to the overlying mountain wave. This increased variability alone represents MKI. Due to greater mixing, the katabatic flow jet is less well defined, located at a higher elevation and, at times, flow is dominated by mountain-wave momentum. The greater mixing also prevents the development of very low near-surface temperatures in REAL, thereby reducing the near-surface katabatic forcing mechanism. We note also that the magnitude of u of REAL on the plains is, with the exception of the first few hours when katabatic flows are building in magnitude, almost exclusively between that of MWO and KFO for a given height above ground until about

hour 8.5. At this point the katabatic flow in REAL, due to persistent mixing by the flow aloft and occasional rotor activity in the lee of the mountains, deepens and its jet rises. Therefore, the flow at 250 m AGL is higher than either MWO or KFO (Fig. 8c) with weaker westerly momentum remaining at 50 m AGL.

By intercomparing time series of u and w at two heights, three canyon-relative locations and between the three simulations here and further of v and θ in Poulos (1996), we have determined that

1) Nearer to the crest of the Rockies, the upper canyon u shows that REAL tended toward the MWO solution at both the 250 and 50 m levels.
2) In the first 5 h of the simulations REAL had the strongest upper-level, upper canyon winds due to intensified stratification and relatively stronger lee-side acceleration due to radiative cooling compared to MWO (cf. Part I).
3) In the latter part of REAL, v becomes highly variable on the microscale [O(1 min.)] for an hour. During this time the wind fields oscillate nonlinearly between the flow magnitudes of the KFO and MWO solutions and correspond with increased wave amplitude and breaking aloft. This effect is not seen in MWO, from which we understand one effect of MKI.
4) Regarding stratification in the upper canyon at 50 m AGL, REAL closely follows that of KFO, but at 250 m the temperatures are cooler because some cold air is mixed to higher altitudes.
5) While the down-canyon flow eventually accelerates to over 15 m s^{-1} in REAL and KFO as canyon topography converges, in MWO the relatively longer wavelength of its mountain wave (due to the lack of radiative cooling) creates weaker winds at this point.
6) Lower canyon winds in REAL are found to be most similar to that of KFO, implying that katabatic forcing dominates mountain-wave forcing at this deep canyon location.
7) On the plains, the temperature of REAL at 50 and 250 m AGL steadily cools—even more so than KFO—due to additional mixing caused by the overlying mountain wave and causes the katabatic flow jet to be weaker and more elevated than in KFO. Dynamically, this is understandable because the jet location appears where the sum of positive pressure gradient forcing due to cooling and negative frictional forcing is maximized.

b. Vertical integrals

Vertical integrals taken at regular intervals through a simulation can be used to summarize time evolution, vertical atmospheric structure, mass transport, circulation strength, and model trends. This section summarizes our analysis of vertical (column) integrals (Fig. 10) from each of the three simulations for horizontal mass flux and heating per unit area at different simulation times. Vertical integrals of zonal mass fluxes are taken upward and can be calculated for a given grid location, n, within a given model column per unit area as

$$F_{un} = \sum_{k=1}^{n} \rho_k u_k \Delta z_k, \tag{1}$$

where k references the vertical grid element, ρ is density, and Δz is the vertical height of a grid element. The integral of the heat content is calculated relative to the heat content at the initial time per unit area, θ_{k0}, and is summed downward. In this case, cooling is indicated by positively sloped lines and is written as

$$H_{\theta n} = c_p \sum_{k=n}^{1} \rho_k (\theta_k - \theta_{k0}) \Delta z_k, \tag{2}$$

where c_p is the specific heat of dry air at constant pressure. Note, further, that for brevity, only the u and θ integrals calculated for the lower canyon point will be discussed.

The relative similarity of panels I(b) and I(c) in Fig. 10, and the relative dissimilarity of panel I(a) from these is the first immediately apparent quality of the u mass flux comparison in Fig. 10. This difference is caused by the strong mountain-wave flow in REAL and MWO and the lack thereof in KFO. Mass flux at the uppermost levels is more than 5 times stronger in panels I(b) and I(c), than in panel I(a), at 3 h. This difference diminishes toward the end of the simulations, however, as easterly momentum influences the calculations at this point in the grid 5 domain. By 1200 UTC in MWO the integrated mass flux becomes negative, indicative of this gradual transition. In contrast, the integrated mass flux of REAL never reaches zero indicating a net eastward transport of mass at all times. While the sum of Figs. 10I(a),(b) clearly does not equal Fig. 10I(c), the addition of radiative cooling in REAL obviously alters the mass balance of the Front Range flow. For most of REAL the positively sloped line indicates increasing net westerly flux with height, with the most notable exception appearing at the end of the simulation. By comparison, the u mass flux integral of KFO has a stronger negative slope aloft, indicative of the easterly return flow above the westerly katabatic current. Therefore, one of the modifications made to katabatic flow by an overlying mountain wave is to mask

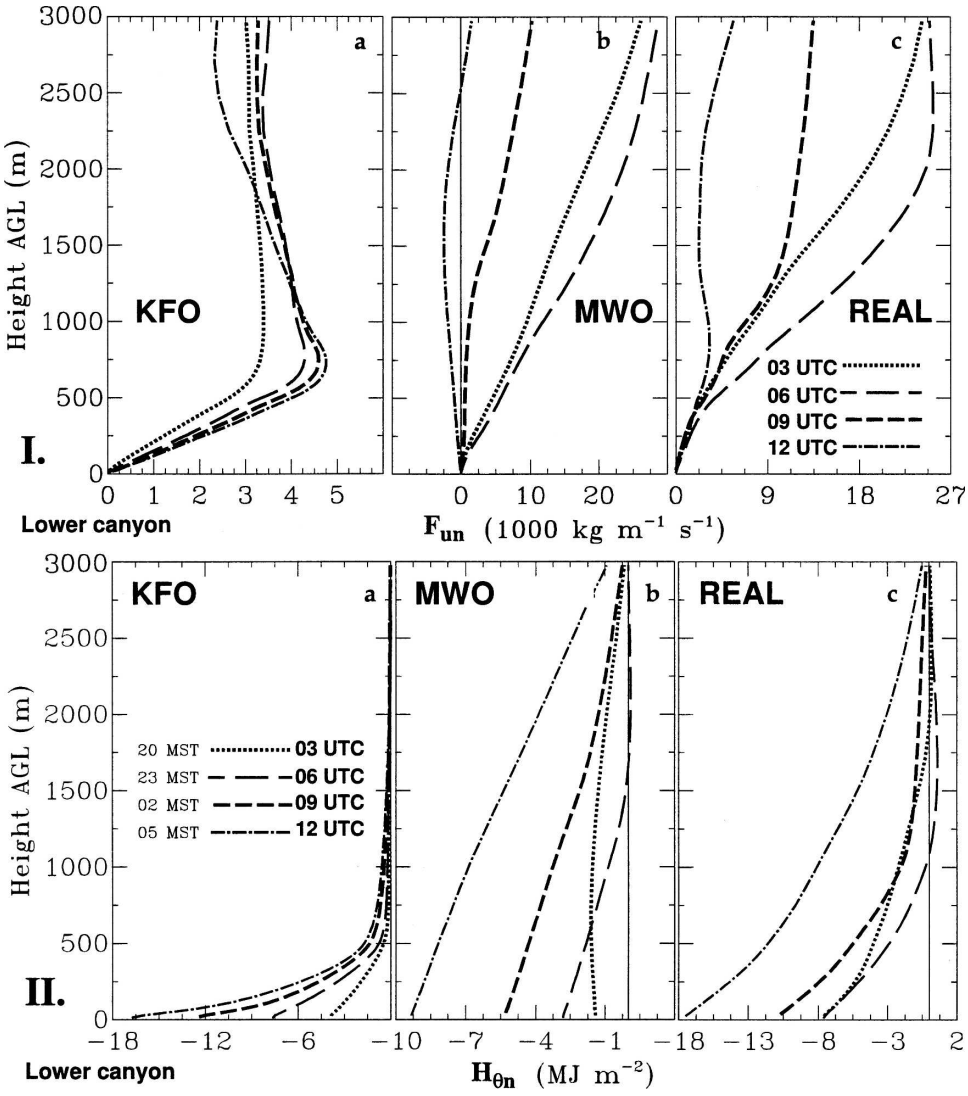

FIG. 10. The vertical integrals of I) F_{un} (1000 kg m^{-1} s^{-1}) and II) $H_{\theta n}$ (MJ m^{-2}). The times shown are 0300, 0600, 0900, and 1200 UTC for (a) KFO, (b) MWO, and (c) REAL. The integrals were performed at point 19 (lower canyon) in Fig. 2.

the return current. By 1200 UTC in REAL, however, a weak return flow does develop as weakening westerly momentum creates a more favorable environment for return flow to be revealed.

The integrals of w (not shown) confirm that radiative cooling has a strong effect on mountain-wave evolution overnight. Without radiative effects, the mountain-wave vertical flux profile evolves from net upward flux at 0600 UTC with little contribution aloft to net downward mass flux at 0900 UTC with little contribution aloft to net upward mass flux throughout the 3000-m integral by 1200 UTC. With radiative effects in REAL, the vertical mass flux evolution is much different. The mountain-wave amplitude is modulated so strongly by developing overnight stratification that at 0300 UTC REAL places the descending portion of the mountain wave over this location (net negative downward mass flux) where MWO places the upward portion of the wave over this location. In the upper canyon (not shown), the vertical mass flux is negative throughout REAL and MWO consistent with a strong stationary wave descending the east side of the Continental Divide. That the mass flux in REAL is of greater magnitude than MWO can be attributed to the stronger stratification and therefore accelerated lee flows in REAL overnight.

As expected, the vertical integral (taken downward) of heating in time for KFO shows large, steady cooling

[Fig. 10II(a)]. The values shown here are somewhat large at the two later times shown because of the excessive cooling problem described in section 3d (the grid point at which these integrals were taken was not the region of greatest temperature error). Regardless, this behavior is intuitive and shows significant cooling through the depth of a ~650-m-deep katabatic layer. MWO also shows significant cooling in time but through a far deeper layer. An analysis of the terms affecting θ indicates that this is primarily due to advection. REAL shows characteristics of both sensitivity simulations; like KFO (as valid for the first two times shown), the strongest cooling in REAL is confined to the lowest atmospheric levels, whereas more like MWO, the depth of cooling in REAL is greater. We therefore conclude that the mountain wave has the overall effect of mixing cooling to a greater depth than would be achieved without active mountain-wave dynamics. Conversely, radiative forcing strengthens the cooling in the lower layers of the atmosphere, increasing the stratification, and causing greater adhesion of the mountain wave to the topography (see also Part I). Because the strongest mountain-wave momentum is thereby confined to a smaller depth, the resulting wind speeds are higher downwind of the Continental Divide, which further enhances the ability of the mountain wave to mix out cool air that otherwise would collect in the valleys.

c. Time series of modeled forcings

Although cross sections, time series of model variables, and integrated fluxes, as described in the previous sections, reveal a considerable amount of information about MKI, still more revealing information about the specific forcing dynamics of MKI can be ascertained from the terms that comprise the equations of motion. To extract this information from a three-dimensional primitive equation numerical model, such as RAMS, is most difficult for each model variable of interest (u, v, w, θ, TKE, and π) at each time step and creates enormous model output. To constrain this problem we limited our term extraction to the grid nodes annotated numerically in Fig. 2 every 2 min (every $2\Delta t$ on grid 1), and the plots were created where all terms of any balance equation were on the right-hand side. Thus, in the figures that follow the line indicating the total forcing or tendency per unit mass, such as $\partial u/\partial t$, are the sum of the other terms shown.

The extracted forcing terms shown here are derived from the numerically discretized of the compressible, three coordinate equations of motion utilized in RAMS (following Tripoli and Cotton 1982):

$$\frac{\partial}{\partial t}(\rho_0 \overline{u}_i) + \frac{1}{a}\frac{\partial}{\partial x_j^*}(ab^{ij}\overline{p}') + \rho_a' g \delta_{i3} = -\frac{1}{a}\left[\frac{\partial}{\partial x_k^*}(ab^{jk}\rho_0 \overline{u_j u_i}) - \overline{u_i}\frac{\partial}{\partial x_k^*}(ab^{jk}\rho_0 \overline{u_j})\right] - \frac{\rho_0}{a}\frac{\partial}{\partial x_k^*}(ab^{jk}\overline{u_i'' u_j''}) - \overline{r_T} g \delta_{i3} + \varepsilon_{ijk} f_j \overline{u_k'}, \quad (3)$$

where $i, j, k = 1, 2, 3$ and a and b are coordinate transformation coefficients inherent in the use of terrain-following coordinates (Clark 1977). In (3), ρ_0 is reference state density, $\overline{u}$ is mean velocity, p is pressure, x^* is the terrain-following coordinate, ρ_a is the density of dry air, g is gravity, δ_{ij} is the Kronecker delta function, u'' is the subgrid-scale velocity, r_T is the total water mixing ratio (comprised of vapor, liquid, and ice mixing ratio, depending on the complexity of cloud microphysics used), ε_{ijk} is the permutation symbol, and f is the Coriolis acceleration. The terms in (3) from left to right are 1) local time rate of change of momentum, 2) the pressure gradient acceleration, 3) gravitational acceleration of dry air, 4) the advection of momentum (written as the difference between a flux divergence and momentum divergence term to improve numerical accuracy), 5) turbulent momentum flux contribution parameterized using K or eddy-viscosity closure, 6) gravitational acceleration due to the density of suspended total water, and 7) the Coriolis acceleration. Advective and source terms are time differenced using a hybrid leapfrog (for momentum)/forward (for scalars) formulation and Asselin filter. Turbulent quantities are time differenced using a forward scheme and acoustic terms utilize a forward–backward semi-implicit scheme over a smaller Δt than used for the other terms (time splitting; Pielke 1984). In space, derivative terms are differenced with fourth-order accuracy in flux conservative form (Pielke et al. 1992).

1) LOWER CANYON, 50 M ABOVE GROUND LEVEL

In Fig. 11 the terms in (3) for $\iota = 1$, $\partial u/\partial t$, for the lower canyon point are plotted as a 4-point running mean from 2-min. sampled data (the contribution from numerical smoothing schemes, labeled "Various" in Fig. 11, and a residual are also shown). Figure 11a for KFO shows that the positive u of katabatic wind in the lower portion of Eldorado Canyon at 50 m AGL is forced by the pressure gradient as balanced primarily by advection of weaker westerly momentum and somewhat more weakly by turbulent forcing. In a Lagrangian frame, this is consistent with $\partial u/\partial t > 0$ or accelerating down-canyon flow. This balance, for the underside of the quasi-katabatic flow jet, compares fa-

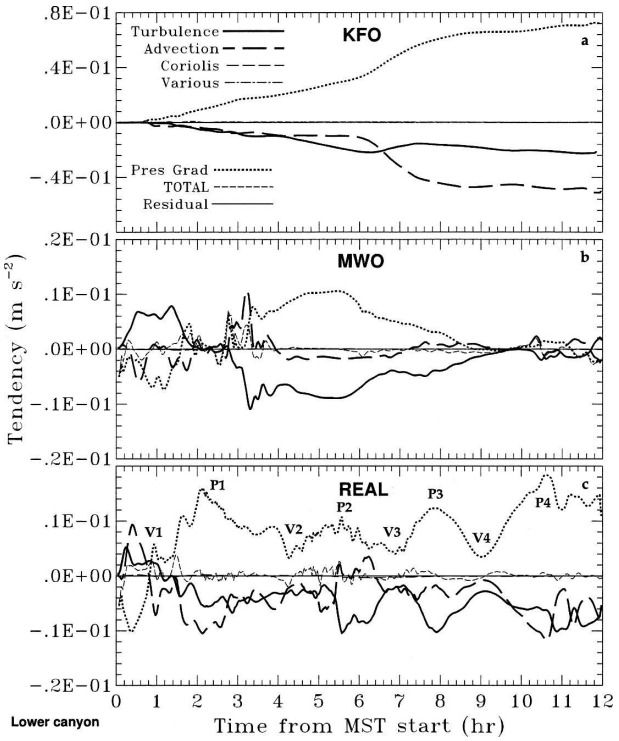

FIG. 11. Terms of the conservation of u momentum equation for the 3–4 Sep 1993 case night for (a) KFO, (b) MWO, and (c) REAL comparable to Fig. 8b. Data are shown as an 8-min running average of 2-min data for the lower canyon point (19 in Fig. 2) at 50 m AGL. The P and V labels in (c) indicate maxima and minima in the PGF, respectively, and can be compared to the same indicators in Fig. 12.

vorably with the large-eddy and mesoscale modeling momentum balance found by Skyllingstad (2003) and Smith and Skyllingstad (2005). Small, positive acceleration of westerly flow occurs during the 1–4-h period from model start, and thereafter the flow is essentially balanced at this level. Note that the line indicating total local tendency, $\partial u/\partial t$, is only slightly positive and, on the scale of this plot, is hardly noticeable. This fact is a testament to the robust balance of forces occurring in the evolution of katabatic flows. Throughout the latter 11 h of the 12-h period the PGF increases in response to continuous turbulent transfer of radiatively cooled air upward from the surface, with a strong increase from 6.5 to 8.5 h. During this time, strong cooling occurs, and the horizontal PGF therefore increases as the local pressure at this elevation MSL becomes larger than that in the free atmosphere at the same level.

Figure 11b shows the model forcing of u at the same grid point but for MWO. The magnitude of the forces, at their maximum, is approximately 6 times smaller than those in KFO after 6 h (note the scales change between panels in Fig. 11). This is, in part, due to the excessively cold air that develops in KFO, which causes a large horizontal PGF to develop after 6 h. MWO develops a nearly neutral low-level atmosphere driven by boundary mixing. Clearly, the varying flow over the Continental Divide causes a likewise variable flow condition in this portion of the canyon. Generally, the MWO total tendency is larger and more noticeable than in KFO, with its sign determined by the local and more variable advective forcing. For most of the 12-h period turbulence balances the PGF, with adjustments to existing advective acceleration. This balance is particularly evident during a relatively steady period from 3 to 8 h. This period corresponds to increased westerly flow and a somewhat larger PGF therefore exists.

The combination of mountain-wave and katabatic forcings creates, in Fig. 11c, a more variable state than exists with either forcing individually. This fact, in and of itself, shows that MKI affects the dynamics of both phenomena significantly and nonlinearly. The magnitude of the terms in (3) is much closer to that of MWO. That the katabatic forcing has a significant effect on the total forcing is most noticeable in the larger average and absolute value of PGF in REAL relative to MWO. The PGF in REAL, for instance, is consistently large and positive after hour 1, whereas MWO is comparably large during only the 3–7-h period (Fig. 11b). Also, during the 3–7-h period in MWO the PGF is smoothly varying, but with radiative cooling in REAL the behavior becomes variable and erratic obviating the nonlinear evolution of the combined phenomena. Overall, similar to KFO but with much larger magnitude, the force balance in REAL is dominated by a positive pressure gradient acceleration and negative advective and turbulent acceleration. Consistent with this balance, katabatic-like flows are evident at this level, despite the relatively larger variability of the terms compared to KFO. Down-canyon of this point, katabatic-like flow is evident in REAL, but it is of greater depth and resides in thermal atmospheric stability of lesser strength than in KFO. This more elevated structure is caused by larger mixing due to the varying overlying mountain wave and verifies some of the conclusions in Part I. Given the far more variable evolution of this katabatic-like flow it is aptly described as a combination of katabatic, mountain wave, and other flows generated by the nonlinear interaction of the phenomena.

Another important aspect of Fig. 11c is the routine occurrence of a peak and valley in the PGF at the meso-β scale [O(1 h)] interval. These meso-β timescale features are labeled "P1" through "P4" and "VI" through "V4," respectively, as shown in expanded detail in Fig. 12 for u. East–west sections of the atmospheric structure in Eldorado Canyon on grid 5 that

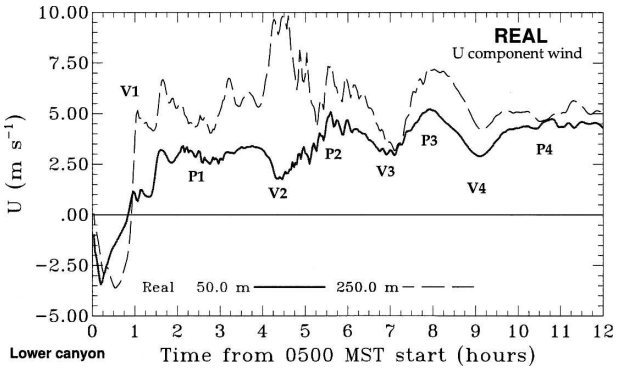

FIG. 12. An expanded scale plot of u (per Fig. 8b) at the lower canyon location (point 19 in Fig. 2) for 12 h during REAL. The P and V labels correspond to the maxima and minima of PGF shown in Fig. 11.

correspond to the times of V2, P2, V3, and P3 are shown in Figs. 13a–d, respectively. It is clear, based on the relatively high magnitude of the PGF at P1 (0.016 m s^{-2}) compared to the near-zero value for MWO and the 0.008 m s^{-2} value of the same in KFO, that a nonlinear combination of mountain wave–induced pressure forcing and radiatively induced pressure (katabatic) forcing is present. At time P1 at this location, not only has cooler denser air begun to accumulate and create a katabatic-type horizontal pressure gradient, but also the surface pressure forcing caused by the vertical structure of the mountain-wave system aloft locally increases the near-surface pressure. As a consequence, the combined effect leads to a local maximum in the horizontal PGF. Lower altitude winds measured farther downwind, however, experience a smaller change (Fig. 9c) because the mountain-wave system has separated from the topography, leaving relatively quiescent lower stability air beneath (alternatively, negative turbulent and advective forcing offsets the large value of PGF). Following our results from Part I, we note that the separation point of the wave and its overall evolution are impacted relative to MWO in REAL due to radiative cooling and katabatic forcing.

Each of the labeled peaks and valleys in Figs. 11c and 12 can be explained in a similar manner as different surface pressure gradient forcings are imposed by the evolving mountain-wave structure above this horizontal position in time (Fig. 13). Figure 12 isolates the u time evolution at the 50- and 250-m AGL level for REAL from Fig. 8b for easier evaluation. In Fig. 12, the meso-β scale maxima (P labels) and minima (V labels)

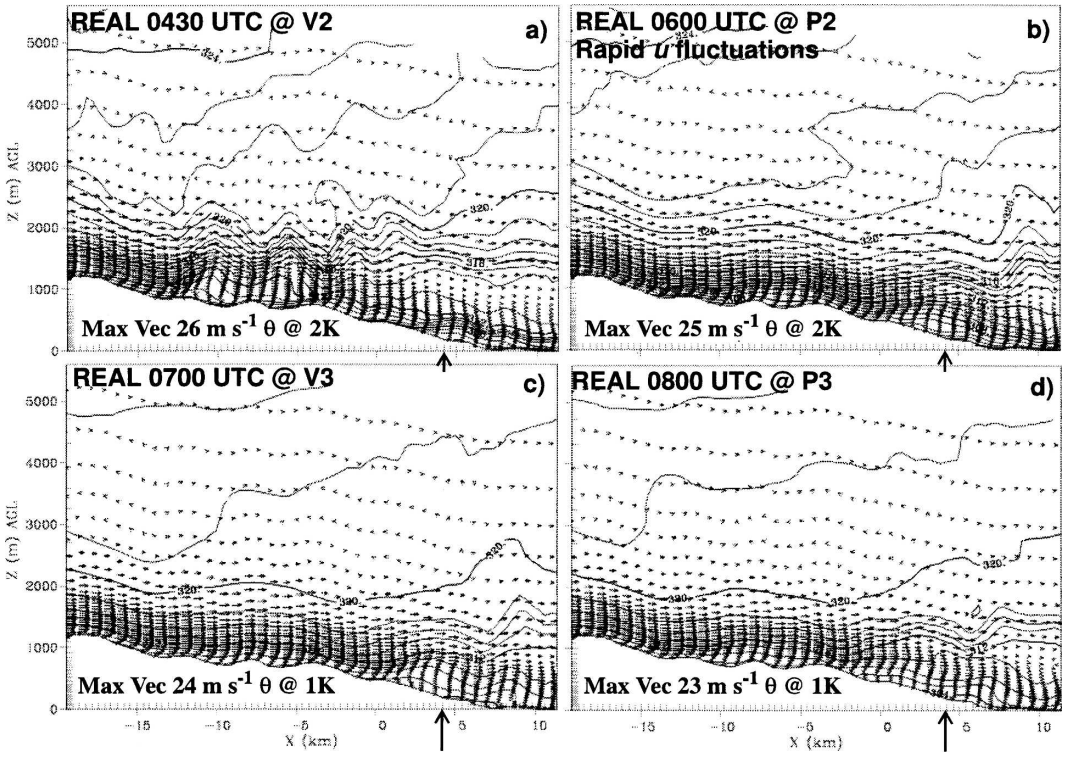

FIG. 13. Cross sections in the x–z plane ($y = -2.2$ km) showing the wave structure in θ and velocity vector structure of the atmosphere in Eldorado Canyon at the times V2, P2, V3, and P3, respectively, as identified for the lower canyon in Figs. 11 and 12. Arrows indicate the horizontal position of the lower canyon point so that the overlying spatial atmospheric structure at a given time can be related to the time evolution.

of the mountain wave–influenced PGF are reflected as 1–3 m s^{-1} mesoscale fluctuations in partially katabatic, partially wave influenced wind speed [an increase (decrease) in wind speed generally occurring where the PGF is high (low)].

One might ask whether the O(1 h) undulations in PGF shown in Fig. 11c are caused by changes to katabatic forcing, since the MKI is an inherently nonlinear process. An alteration of the katabatic forcing would be reflected as oscillations of temperature that correlate to those in Figs. 11 and 12, but though some oscillations do exist (not shown), as would be expected for an evolving flow, these oscillations are quite small and not correlated to the PGF oscillations. Referencing Fig. 13, the atmospheric state at the time of V2, P2, V3, and P3 (see Figs. 13a–d, respectively) above the lower canyon point clearly changes. These changes are most evident in the waves embedded in the near-surface statically stable layer, where gravity wave–induced atmospheric pressure changes are efficiently transmitted to the surface as wave and flow structure evolves aloft. Although it is not possible to ascribe a particular wave system structure in Figs. 13a–d to a particular maximum or minimum in PGF in Figs. 11c and 12, it is clear that the overlying wave structure is evolving with time. That these O(1 h) oscillations are not numerical artifacts is evidenced by the lack of similar oscillations in KFO and MWO. We conclude then that evolving pressure forcing from an overlying mountain-wave system can drastically influence the otherwise steady pressure gradient forcing in katabatic flow (Fig. 11a), inducing significant variability on the meso-β scale. Given that the evolving cooling and katabatic flow affect the mountain wave through Fr, and the evolving shear and surface pressure forcing of the wave affect the katabatic flows (Figs. 3a–c), it is clearly a mutual nonlinear interaction. The PGF in Fig. 11c does not increase in magnitude throughout the 12-h simulation, as seen in Fig. 11a, because the increased mixing prevents continuous cooling.

We also note that, similar to the idealized simulations in Part I and as described in section 4a, superimposed microscale [O(1 min)] fluctuations in the near-surface (perhaps katabatic, perhaps not readily identifiable as katabatic flow due to the disturbance) flow correspond to those periods where rapid wave evolution of short wavelength features and mountain-wave breaking occur above a particular horizontal location (Fig. 13). Slower time scale, more smoothly varying flow evolution corresponds to times where mountain-wave flow is not evolving rapidly, such as in Fig. 13d for point P3. From Fig. 12, these microscale fluctuations occur from 2 to 3.25 h and from 4.5 to about 7 h. Figure 13a at 0430 UTC represents the conditions entering the second period of more rapid variability and Fig. 13b represents the time of P2 during the period of superimposed fluctuations. Figure 13a (and subsequent plots, not shown) indicates that this was a period where small λ waves (a few kilometers) were evolving and propagating through the lower canyon. Figure 13b shows that an overturning, relatively high amplitude, short λ feature has formed aloft in the immediate vicinity of this lower canyon point.

From this simulated behavior we conclude that the near-surface realization of the dynamic pressure forcing from the integrated structure of an overlying mountain-wave system directly influences the development and subsequent level of variability found in the evolution of katabatic winds. Acoustic sodar measurements during the ASCOT experiment (Part I, Fig. 3; Poulos 1996) detected O(1 h) fluctuations in katabatic flows but were insufficient to verify the natural occurrence of this phenomenon because insufficient mountain wave–level thermodynamic measurements were made. Coulter and Gudiksen (1995), however, confirm the variability of katabatic flow speeds with differing ambient flow speed over longer time scales during the ASCOT study.

2) LOWER CANYON, 250 M ABOVE GROUND LEVEL

At higher levels, such as 250 m AGL in the lower canyon (see Fig. 14) the relationship of mountain-wave pressure forcing to near-surface winds is somewhat masked by the momentum of the mountain wave itself and less radiatively driven cooling. At this level in KFO (Fig. 14a), where katabatic flow is less subject to the retarding effects of surface friction due to underlying stratification, a primarily two-way force balance is found between the positive PGF and the advection of slower upstream air into the location (e.g., Skyllingstad 2003). This is an advective gravity flow in the Mahrt (1982) classification. Aside from the steady growth of each part in the $\partial u/\partial t$ force balance, there is no small time-scale variability in the various accelerations over time. In MWO, where radiatively induced stable layers and hence frictional decoupling cannot occur, turbulence remains a significant factor in the force balance for u winds (Fig. 14b). The magnitude of the negative turbulent forcing for this altitude in MWO is somewhat smaller than that at the surface, however, the PGF is similar (a jetlike structure in this case forms between 3 and 8 h; see Fig. 3b). Depending on the speed of winds approaching this horizontal location, which depends on the incoming upstream flow impacting the barrier, topographic interaction, and thermal structure, advection plays a variable role in $\partial u/\partial t$.

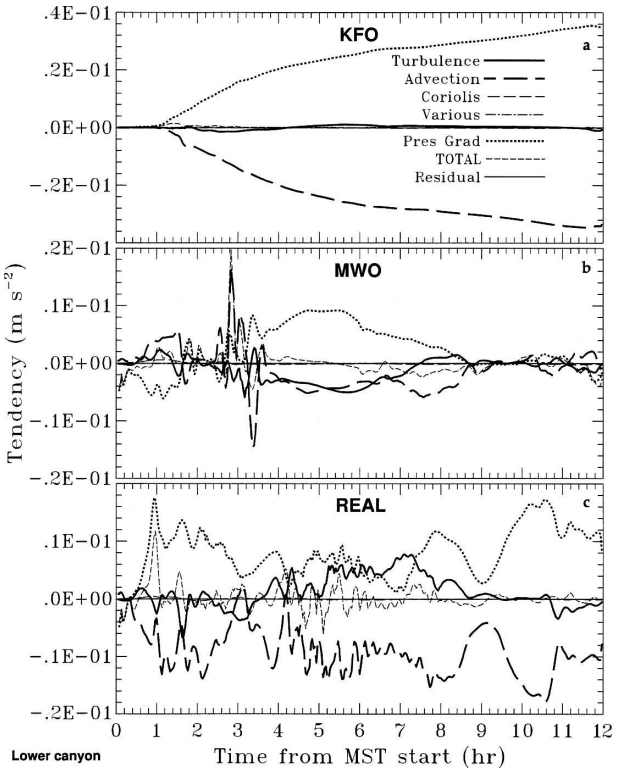

FIG. 14. Same as in Fig. 11 but for 250 m AGL. Compare to Fig. 8b.

For REAL (Fig. 14c), a highly variable force balance is depicted with many similar features to that of the 50-m AGL plots in Fig. 11c. The first and foremost similarity is the existence of maxima and minima in the PGF. However, turbulence, which played a primarily negative role at the 50-m AGL level, here is occasionally negative but also positive for the 4–9-h period. The 250-m AGL level is somewhat closer to the level of strongest wave momentum and shear in the overlying mountain wave and thus is more influenced by it. During this period, discerning what is katabatic flow and what flow is governed by mountain-wave dynamics is essentially impossible. Clearly, some katabatic forcing is occurring due to the similarity in force balance between KFO and REAL in Fig. 14, but the downward turbulent intrusion of high momentum air also undoubtedly contributes to the flow here. Katabatic flow seems to be intermittently dominant depending on the strength and phase of the overlying mountain wave, with most influence occurring in the first and last 3 h of the 12-h simulation. The microscale oscillations superimposed on the longer time-scale oscillations in REAL at this level (Figs. 12 and 14c) are consistent with those found at the 50-m level.

3) UPPER CANYON, 50 M ABOVE GROUND LEVEL

In the upper canyon (point 30 in Fig. 2), dynamical evolution (not shown) differs significantly from that in the lower canyon, most significantly by the role of the mountain wave, but reinforces our notion of MKI. In this case, as west–east katabatic flow grows in strength from the Continental Divide slope on the west side of this location and crosses the canyon axis, advection becomes a positive u forcing compared with consistently negative forcing in the lower canyon at 50 m AGL (Fig. 8a). Overall, the size of the forcing on u is considerably smaller than that in the lower canyon for two reasons: 1) the upper canyon is more north–south oriented so that katabatic forcing is primarily in the v component, and 2) the lower canyon experienced excessive cooling in the latter 6 h of the simulation; prior to that time lower canyon katabatic forcing is much smaller and realistic. In MWO, the upper canyon tendency time evolution is consistent with flow dominated by mountain-wave momentum (scouring). That is, this grid node lies in the topographically anchored, downward phase of the primary wave caused by upstream northwesterly flow, though somewhat protected by the local canyon orientation. As the upstream flow surmounts the barrier and accelerates down the east side of the Continental Divide a positive horizontal PGF drives the flow. Positive forcing is also contributed from turbulent diffusion from 2 to 6 h as strong shear induces mixing and therefore higher momentum air to be transferred down to this level. The evolution of the u in REAL (not shown) at this elevation is somewhat similar to that of MWO, evidencing domination by mountain-wave dynamics in the upper canyon location. This is evident in the magnitude of the PGF driving u flow. If the forcing were purely katabatic at this level, KFO shows that pressure gradient tendency would be able to achieve a maximum of ~ 0.01 m s^{-2}, whereas a value approximately 6 times this is achieved in REAL, similar to MWO. The strong mountain-wave momentum and shear prevent the development of stratification as strong as that in KFO. However, the stratification that does develop causes the mountain wave to be confined to a shallower depth and thereby adhere to the mountainside somewhat more than in MWO. Thus, radiative cooling serves to increase the mountain-wave momentum presence near the surface, allowing greater domination of the flow by the mountain wave than would otherwise occur.

5. A conceptual model for MKI

Toward understanding the causes of variability in complex terrain katabatic flows, it was hypothesized herein that a frequently occurring complex terrain phe-

nomenon, topographically induced internal wave evolution, would impact the variability and evolution of katabatic flow. It was further hypothesized that this interaction would be complicated by the mutual evolution of the two phenomena, which is inherently nonlinear. Analysis of our idealized topography (Part I) and realistic topography simulations herein support these hypotheses and provide sufficient substance for the development for a conceptual model for mountain wave–katabatic flow interaction. The specific case study on which this conceptual picture is based resides in the nonlinear, Fr = 0.45, regime. Given the half-width of the Rocky Mountain barrier, this flow was on the large-scale hydrostatically (Durran 1990) and on the scale of local peaks and valleys nonhydrostatically. Although the simulations herein were three-dimensional and clearly the flows undergo complex mutual three-dimensional interaction, the effects found were most clearly represented in the along-flow direction in canyons, plains, and slopes (see also Part I). The conceptual picture is therefore drawn in two-dimensions.

The conceptual model proposed below focuses primarily on the result of MKI on the near-surface flow, which is generally a nonlinear combination of wave-induced and radiatively driven forcing, rather than attempting to pictorially represent the wide array of nonlinear wave responses possible aloft. While it was clear in this study that the upper-level evolution of the overlying wave flow was influenced by evolving the atmospheric structure when subjected to radiational cooling, the analysis was insufficient to generalize the effects and differentiate them from current understanding of mountain-wave instability, and thus it is left for future study. A firm basis for such future studies exists in the voluminous literature describing nonlinear topographically induced waveforms and associated instability (e.g., Lester and Fingerhut 1974; Blumen and McGregor 1976; Brighton 1978; Clark and Peltier 1984; Bannon 1985; Bannon and Zehnder 1985; Durran 1986; Lee et al. 1987; Bacmeister and Schoeberl 1989; Reisner and Smolarkiewicz 1994; Lee et al. 1989; Weissbluth and Cotton 1989).

a. MKI: Mountain wave–induced turbulence effects on katabatic flow

In this portion of the conceptual model (Fig. 15), the general categorization as "turbulence effects" is used to encapsulate those mountain wave–induced effects on katabatic flow that occur through diffusion or mixing processes, most often as regards thermal stratification. ASCOT observations, previous work, and numerical simulations show that katabatic flows develop within strong (i.e., $d\theta/dz > 10$ K km^{-1}) surface-based thermal stratification, which, itself, develops because of cooling driven by radiative flux divergence and turbulent mixing, such as depicted conceptually in the upper panel of Fig. 15. Since this cooling is also responsible for the buoyancy forces that drive katabatic flow, the depth of this cool air, insofar as it is cooler than air in the free atmosphere at the same altitude, defines the depth of the katabatic flow layer. Therefore, alterations to this thermal structure by external influences, such as mountain waves, cause changes in katabatic flow depth and strength.

Compared to katabatic flow in an undisturbed atmosphere, this investigation, inclusive of Part I, has shown that when a mountain wave is present thermal stratification associated with katabatic flow is weaker and often deeper as depicted in the bottom panel of Fig. 15. As a consequence of this deeper layer, katabatic flows are also deepened in most cases. Correspondingly smaller differences in temperature between the katabatic layer air and the free atmosphere cause the katabatic flow jet speed to decrease, and its vertical location to increase somewhat. However, if mountain-wave flow is strong enough in a particular region of interest, mountain-wave momentum will completely dominate the near-surface atmosphere and scour katabatic flow (Fig. 15, upper slope of bottom panel). Radiative cooling still occurs in the scoured zone, although the vertical thermodynamic structure there is primarily determined by that in the descent of isentropes in the downward phase of the mountain-wave. The scoured zone can be defined by the distance downslope to the separation point of the mountain-wave. Using the results from Part I of this study, we expect then for higher Froude number that scouring proceeds to a greater distance downslope. Even in the case of Fr = 1.0, a case where theory provides that the mountain wave may descend the entire slope length, katabatic flow can develop in strongly cooling lower altitudes if stratification becomes strong enough to prevent mountain wave penetration. Considering Part I further, we find that for $\sim 0.40 < \mathrm{Fr} < 1.0$, scouring is still significant along the upper slopes of the barrier, but below the separation point flow it is quiescent enough to allow the development of katabatic flow. At low Fr the interaction is much different (see Part I).

b. MKI: Mountain wave–induced pressure effects on katabatic flow

An intriguing result of this study is that pressure effects caused by the evolving mountain-wave system aloft can alter katabatic flow speeds, even if the notable mountain-wave features are rapidly evolving, propagating, or breaking above the katabatic flow (Fig. 16). In

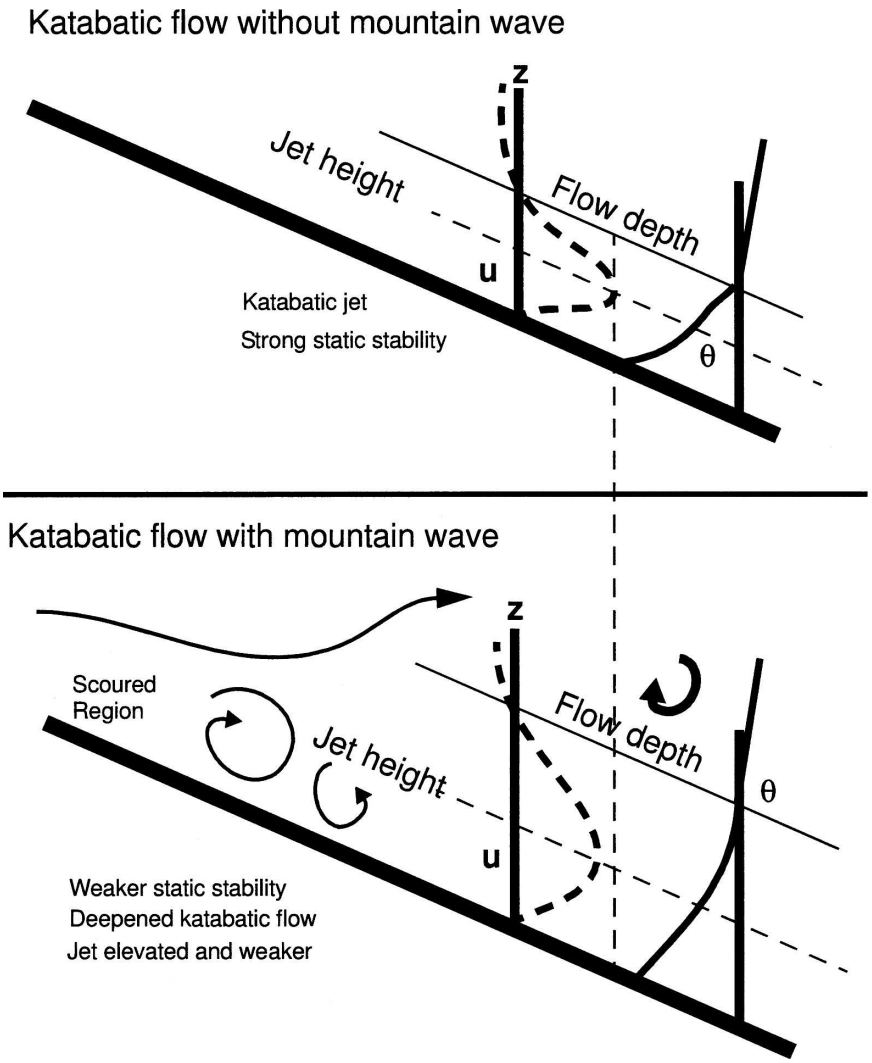

FIG. 15. A schematic diagram of the influence of turbulence induced by a mountain wave descending into leeside katabatic flows. (top) The katabatic wind speed and static stability without mountain-wave influence. (bottom) The katabatic flow structure with a mountain wave; upper slopes are scoured while the vertical structure of the katabatic flow on lower slopes is altered significantly by increased shear or other effects.

this conceptual model, for a given atmospheric condition, a nonlinear mountain-wave flow will often develop a complicated tropospheric wave structure downstream of the barrier, depicted by the wavy upper-level lines in both panels of Fig. 16. In the immediate vicinity of the barrier it is well known that the upstream side of the mountain will develop a wave-induced local high pressure, whereas in the lee there will be relatively low pressure. Farther in the lee, however, after the mountain wave separates from the barrier, any number of gravity wave structures can exist in the vertical, from strong ducted lee waves to gently propagating evanescent waves depending on the vertical profile of temperature and wind (Fig. 13). Since the effect of this complicated wave structure on the surface pressure is determined by the net pressure disturbance induced by the mountain-wave system above a particular point (and possibly by divergent effects not included in this conceptual model), the mountain wave–induced surface pressure effect will vary with horizontal location. We find through our numerical studies herein that this effect can cause horizontal pressure variations of $O(1\ \text{hPa})$.

Since katabatic flow is a surface-based, pressure gradient–dependent phenomenon, it is affected by these alterations of surface pressure gradient caused by the mountain wave, even if the wave undulations are elevated above the flow. Note in the upper diagram of

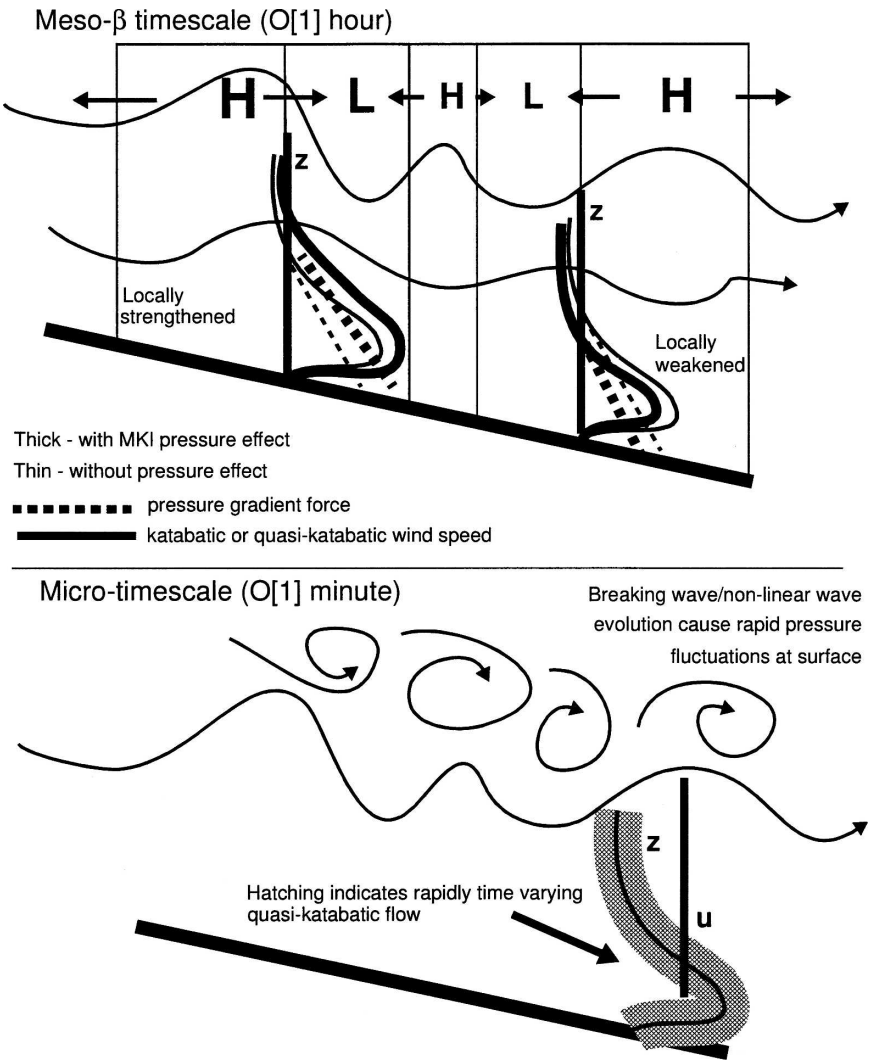

FIG. 16. Schematic diagrams of the two dynamic pressure effects of mountain waves on katabatic flow. (top) Depending on location, katabatic flow can be either strengthened (upper slope case) or weakened (lower slope case) due to the integrated column pressure structure of the mountain-wave system above and the locally induced pressure gradient (arrows). (bottom) A breaking or rapidly nonlinearly evolving mountain wave aloft causes rapid pressure fluctuations, which, in turn, cause rapid katabatic flow fluctuations.

Fig. 16 that the columnwise pressure changes are indicated as discrete highs (H) and lows (L) for clarity, although the system and its surface impacts are nonlinear and three-dimensional. Furthermore, as the mountain wave evolves, the downstream wave structure, and therefore surface pressure perturbation, will change. The PGF and therefore local flow speed can locally strengthen due to the surface manifestation of wave-induced pressure perturbations near the surface as in the upper panel, upper slope case in Fig. 16, and vice versa (upper panel, lower slope). Analyses in this study consistent with this conceptual picture have shown that katabatic flow speeds can be forced to vary by 1–3 $m\,s^{-1}$ through this effect over meso-β [O(1 h)] time scales (Figs. 8 and 11–14). It has also been found that high-frequency oscillations in surface flow can be generated on the microtime scale [O(1 min.)] by pressure perturbations induced by breaking and rapidly evolving wave structure aloft, as illustrated in the lower diagram of Fig. 16. One might speculate, of course, that this effect is not limited to katabatic flow only, as any surface flow would be influenced by such pressure effects.

c. *Final remarks*

The authors wish to emphasize the complicated evolution that exists when radiatively driven katabatic flow

and mountain waves exist together. Oftentimes during the overnight period near the surface these flows are inseparable and indistinguishable. The mountain wave, rather than being a steady-state feature, is constantly changing due to time-varying upstream flow speed and direction, local stratification, and other superimposed natural atmospheric phenomena. Evolving local stratification, which produces the negatively buoyant atmospheric structure required for katabatic flows, is altered by the level of mixing induced by overlying mountain-wave flow. Consequently, katabatic flow structure is altered in a nonlinear fashion depending on the interplay of all these causes of variability. The result is a far more variable stable nocturnal boundary layer in complex terrain than has been generally understood to exist, consistent with sometimes highly variable and therefore confounding atmospheric profiles of these seemingly simple flows (cf. Fujita 1986).

As with many studies, this investigation appears to have broader implications for the study of the atmosphere than originally anticipated. While the MKI phenomenon is found to be an important component of katabatic flow variability, there is no obvious reason why these effects are limited to causing variability only in the NBL. Furthermore, these influences should not be limited to nocturnal periods but are also likely during daytime boundary layer development. Even more generally, the source of the gravity waves causing the boundary layer variability is not limited to those only caused by topographic features. As such, it is perhaps more reasonable to define the mechanism as a component of gravity wave–boundary layer interaction and expect that it is a more general source of variability in atmospheric boundary layer measurements.

Acknowledgments. Thanks are due to the following for their input on this project: Professor Bjorn Stevens, University of California, Los Angeles; Dr. Robert Walko, Duke University; and Dr. Keeley Costigan of Los Alamos National Laboratory. Helpful comments on the manuscript were also provided by Rich Rotunno of the National Center for Atmospheric Research and anonymous reviewers.

REFERENCES

Armi, L., and R. Williams, 1983: The hydraulics of a stratified fluid flowing through a contraction. *J. Fluid Mech.,* **251,** 355–375.

Bacmeister, J. T., and M. R. Schoeberl, 1989: Breakdown of vertically propagating two-dimensional gravity waves forced by orography. *J. Atmos. Sci.,* **46,** 2109–2134.

Baines, P. G., 1979: Observations of stratified flow past three-dimensional barriers. *J. Geophys. Res.,* **84,** 7834–7838.

Bannon, P. R., 1985: Flow acceleration and mountain drag. *J. Atmos. Sci.,* **42,** 2445–2453.

——, and J. A. Zehnder, 1985: Surface pressure and mountain drag for transient airflow over a mountain ridge. *J. Atmos. Sci.,* **42,** 2454–2462.

Banta, R. M., L. D. Olivier, W. D. Neff, D. H. Levinson, and D. Ruffieux, 1995: Influence of canyon-induced flows on flow and dispersion over adjacent plains. *Theor. Appl. Climatol.,* **52,** 27–42.

——, ——, P. H. Gudiksen, and R. Lange, 1996: Implications of small-scale flow features to modeling dispersion over complex terrain. *J. Appl. Meteor.,* **35,** 330–342.

Bleck, R., and S. G. Benjamin, 1993: Regional weather prediction with a model combining terrain-following and isentropic coordinates. Part I: Model description. *Mon. Wea. Rev.,* **121,** 1770–1785.

Blumen, W., and C. D. McGregor, 1976: Wave drag by three-dimensional mountain lee-waves in nonplanar shear flow. *Tellus,* **28,** 287–298.

Bossert, J. E., and G. S. Poulos, 1995: A numerical investigation of mechanisms affecting drainage flows in highly complex terrain. *Theor. Appl. Climatol.,* **52,** 119–134.

Brighton, P. W. M., 1978: Strongly stratified flow past three-dimensional obstacles. *Quart. J. Roy. Meteor. Soc.,* **104,** 289–307.

Buettner, K. J. K., and N. Thyer, 1965: Valley winds in the Mount Ranier area. *Arch. Meteor. Geophys. Bioklimatol.,* **14,** 125–147.

Chow, F. K., A. P. Weigel, R. L. Street, M. W. Rotach, and M. Xue, 2006: High-resolution large-eddy simulations of flow in a steep Alpine valley. Part I: Methodology, verification, and sensitivity experiments. *J. Appl. Meteor.,* **45,** 63–86.

Clark, T. L., 1977: A small-scale dynamic model using a terrain-following coordinate transformation. *J. Comput. Phys.,* **24,** 186–215.

——, and W. R. Peltier, 1984: Critical level reflection and resonant growth of nonlinear mountain waves. *J. Atmos. Sci.,* **41,** 3121–3134.

Coulter, R. L., and P. Gudiksen, 1995: The dependence of canyon winds and surface cooling and external forcing in Colorado's Front Range. *J. Appl. Meteor.,* **34,** 1419–1429.

Derbyshire, S. H., 1999: Boundary-layer decoupling over cold surfaces as a physical boundary instability. *Bound.-Layer Meteor.,* **90,** 297–325.

Durran, D. R., 1986: Another look at downslope windstorms. Part I: The development of analogs to supercritical flow in and infinitely deep, continuously stratified fluid. *J. Atmos. Sci.,* **43,** 2527–2543.

——, 1990: Mountain waves and downslope winds. *Atmospheric Processes in Complex Terrain, Meteor. Monogr.,* No. 45, Amer. Meteor. Soc., 59–81.

Fujita, T. T., 1986: Mesoscale classifications: Their history and their application to forecasting. *Mesoscale Meteorology and Forecasting,* P. S. Ray, Ed., Amer. Meteor. Soc., 18–35.

Jackson, P. L., and D. G. Steyn, 1994: Gap winds in a fjord. Part II: Hydraulic analog. *Mon. Wea. Rev.,* **122,** 2666–2676.

Klemp, J. B., and R. B. Wilhelmson, 1978: The simulation of three-dimensional convective storm dynamics. *J. Atmos. Sci.,* **35,** 1070–1096.

Lee, J. T., R. E. Lawson Jr., and G. L. Marsh, 1987: Flow visualization experiments on stably stratified flow over ridges and valleys. *Meteor. Atmos. Phys.,* **37,** 183–194.

——, R. A. Pielke, R. C. Kessler, and J. Weaver, 1989: Influence

of cold pools downstream of mountain barriers on downslope winds and flushing. *Mon. Wea. Rev.,* **117,** 2041–2058.

Lester, P. F., and W. A. Fingerhut, 1974: Lower turbulent zones associated with mountain lee waves. *J. Appl. Meteor.,* **13,** 54–61.

Mahrt, L., 1982: Momentum balance of gravity flows. *J. Atmos. Sci.,* **39,** 2701–2711.

——, 1998: Stratified atmospheric boundary layers and breakdown of models. *J. Theor. Comput. Fluid Dyn.,* **11,** 263–280.

McKee, T. B., and R. D. O'Neal, 1989: The role of valley geometry and energy budget in the formation of nocturnal valley winds. *J. Appl. Meteor.,* **28,** 445–456.

Olafsson, H., and P. Bougeault, 1996: Nonlinear flow past and elliptic mountain ridge. *J. Atmos. Sci.,* **53,** 2465–2489.

Pan, F., and R. B. Smith, 1999: Gap winds and wakes: SAR observation and numerical simulations. *J. Atmos. Sci.,* **56,** 905–923.

Pan, Z., S. G. Benjamin, J. M. Brown, and T. Smirnova, 1994: Comparative experiments with MAPS on different parameterization schemes for surface moisture flux and boundary-layer processes. *Mon. Wea. Rev.,* **122,** 449–470.

Pielke, R. A., 1984: *Mesoscale Meteorological Modeling.* Academic Press, 612 pp.

——, and Coauthors, 1992: A comprehensive meteorological modeling system—RAMS. *Meteor. Atmos. Phys.,* **49,** 69–91.

Poulos, G. S., 1996: The interaction of katabatic winds and mountain waves. Ph.D. dissertation, Colorado State University, 297 pp. [Los Alamos National Laboratory Publication LA-13224-T, Los Alamos, New Mexico.]

——, and J. E. Bossert, 1995: An observational and prognostic numerical investigation of complex terrain dispersion. *J. Appl. Meteor.,* **34,** 650–669.

——, and S. P. Burns, 2003: An evaluation of bulk Ri-based surface layer flux formulas for stable and very stable condition with intermittent turbulence. *J. Atmos. Sci.,* **60,** 2523–2537.

——, J. E. Bossert, T. B. McKee, and R. A. Pielke, 2000: The interaction of katabatic flow and mountain waves. Part I: Observations and idealized simulations. *J. Atmos. Sci.,* **57,** 1919–1936.

Queney, P., 1948: The problem of airflow over mountains: A summary of theoretical studies. *Bull. Amer. Meteor. Soc.,* **29,** 16–26.

——, G. A. Corby, N. Gerbier, H. Koschmieder, and J. Zierep, 1960: The airflow over mountains. Tech. Note 34, World Meteorological Organization, 135 pp.

Reed, T. R., 1931: Gap winds of the Strait of Juan de Fuca. *Mon. Wea. Rev.,* **59,** 373–376.

Reisner, J. M., and P. K. Smolarkiewicz, 1994: Thermally forced low Froude number flow past three-dimensional obstacles. *J. Atmos. Sci.,* **51,** 117–133.

Saunders, P. M., 1987: Flow through Discovery Gap. *J. Phys. Oceanogr.,* **17,** 631–643.

Skyllingstad, E. D., 2003: Large-eddy simulation of katabatic flows. *Bound.-Layer Meteor.,* **106,** 217–243.

Smith, C. M., and E. D. Skyllingstad, 2005: Numerical simulation of katabatic flow with changing slope angle. *Mon. Wea. Rev.,* **133,** 3065–3080.

Smith, R. B., 1979: The influence of mountains on the atmosphere. *Advances in Geophysics,* Vol. 21, Academic Press, 87–230.

——, 1989: Mountain-induced stagnation points in hydrostatic flow. *Tellus,* **41A,** 270–274.

Song, J. L., R. A. Pielke, M. Segal, R. W. Arritt, and R. Kessler, 1985: A method to determine nonhydrostatic effects within subdomains within a mesoscale model. *J. Atmos. Sci.,* **42,** 2110–2120.

Stein, U., and P. Alpert, 1993: Factor separation in numerical simulations. *J. Atmos. Sci.,* **50,** 2107–2115.

Tripoli, G. J., and W. R. Cotton, 1982: The Colorado State University three-dimensional cloud/mesoscale model-1982. Part I: General theoretical framework and sensitivity experiments. *J. Rech. Atmos.,* **16,** 185–220.

Viterbo, P., A. Beljaars, J.-F. Mahfouf, and J. Teixeira, 1999: The representation of soil moisture freezing and its impact on the stable boundary layer. *Quart. J. Roy. Meteor. Soc.,* **125,** 2401–2426.

Weigel, A. P., F. K. Chow, M. W. Rotach, R. L. Street, and M. Xue, 2006: High-resolution large-eddy simulations of flow in a steep Alpine valley. Part II: Flow structure and heat budgets. *J. Appl. Meteor. Climatol.,* **45,** 87–107.

Weissbluth, M. J., and W. R. Cotton, 1989: Radiative and nonlinear influences on orographic gravity wave drag. *Mon. Wea. Rev.,* **117,** 2518–2534.

Whiteman, C. D., 1990: Observations of thermally developed wind systems in mountainous terrain. *Atmospheric Processes over Complex Terrain, Meteor. Monogr.,* No. 45, Amer. Meteor. Soc., 5–42.

Zängl, G., 2002: Stratified flow over a mountain with a gap: Linear theory and numerical simulations. *Quart. J. Roy. Meteor. Soc.,* **128,** 927–949.